Contents lists available at ScienceDirect

Journal of Magnetism and Magnetic Materials

Velocity-slip boundary conditions and shape factor effects on MHD hybrid nanofluid flow via converging/diverging channels

Mohamed Kezzar [a], Nabil Talbi [a], Mohamed Rafik Sari [b], Abdelaziz Nehal [b], Mohsen Sharifpur [c,d,*], Ravinder Kumar [e], Nima Gharib [f], Wafa Salsoul [g], Haddad Fatiha [g]

[a] Mechanical Engineering Department, University of Skikda, El Hadaiek Road, B. O. 26, 21000 Skikda, Algeria
[b] Mechanics of Materials and Plant Maintenance Research Laboratory (LR3MI), Mechanical Engineering Department, Faculty of Engineering, Badji Mokhtar University of Annaba (UBMA), PO Box 12, 23052 Annaba, Algeria
[c] Department of Mechanical and Aeronautical Engineering, University of Pretoria, Pretoria 0002, South Africa
[d] Department of Medical Research, China Medical University Hospital, China Medical University, Taichung, Taiwan
[e] School of Mechanical Engineering, Lovely Professional University, Punjab, India
[f] College of Engineering and Technology, American University of the Middle East, Egaila 54200, Kuwait
[g] Physical Engineering Department, University of 20 aout 1955, El Hadaiek Road, B. O. 26, 21000 Skikda, Algeria

ARTICLE INFO

ABSTRACT

The most important objective of this research-work is to investigate the impacts of velocity-slip boundary conditions and shape factor of solid nanoparticles on the hydrodynamic behavior of the nonlinear problem of MHD Jeffery–Hamel hybrid nanofluid flow where the mixture $H_2O - C_2H_6O_2$ (50% −50%) was utilized as a base fluid. Using appropriate velocity transformations, the basic partial differential equations arising from mathematical modeling are transformed into non-linear ordinary differential equations. Afterwards, the determined nonlinear equation was numerically solved utilizing Runge-Kutta-Fehlberg 4th–5th order approach featuring shooting technique and analytically with the help of Duan–Rach Approach (DRA). The impact of active factors like Reynolds number, channel half-angle, Hartman number, base fluids nature, hybrid nanoparticles, velocity-slip boundary conditions, shape and Geometry of solid nanoparticles on hybrid nanofluid velocity and skin friction coefficient are visualized and investigated. The minimal local skin friction is found to be obtainable with the nanoparticles of Platelet form and second-order slip model where a reduction of 70% is gained compared to the local skin friction coefficient with spherical nanoparticles when the Hartmann number is higher. Results obtained also reveal that a higher reduction of 69% in local skin friction coefficient intensity is observed for both hybrid phase $(Al_2O_3 - Cu)$ and mixture base fluid $(H_2O - C_2H_6O_2)$ with second-order slip boundary condition model when Knudsen number Kn = 0,08. A comparison was made between the results obtained from this investigation in particular cases and the results obtained via the HAM-based Mathematica package for validation. Also, the obtained analytical DRA data are compared with numerical RKF45 data and the ones represented in the literature. The comparison revealed that the results match perfectly which justifies applicability, validity, and the higher exactness of the adopted Duan-Rach approach.

1. Introduction

Hydromagnetics or Magneto-Hydrodynamics (M.H.D.) is highly known as a branch of science that focuses on electrically conducting fluids dynamics. MHD has different industrial applications like accelerometers, cooling systems designs with liquid metals, crystal growth, flow meters and MHD power production. The first use of M.H.D. term is given by Hannes Alfven [1]. In recent years, several studies have been implemented by different scholars to acquire knowledge about the impact of magnetic field on heat transfer and fluid flow through several geometrical configurations. For example, Zhao et al. [2] studied analytically by employing the method of variables separation the magnetohydrodynamic (MHD) incompressible generalized Maxwell fluids flow under the effect of alternating current electric field through a two-dimensional rectangular micropump. They showed the influence of the electrical oscillating Reynolds number Re, the dimensionless relaxation

time De and the Hartmann number Ha on the velocity evolution. The results agreed with available literature and experimental data.

Satya Narayana et al. [3] investigated the impact of heat and mass transfer on MHD oscillatory flow in an asymmetric wavy channel with chemical reaction and heat source. They observed that the increase of heat transport in oscillatory flow is more pronounced than that occurs in ordinary conduction. Shafiq and Sindhu [4] interested on the effect of both electric and magnetic fields in their contribution focusing on the unsteady boundary layer flow of an incompressible Williamson fluid over a permeable radiative stretched surface. They visualized velocity and temperature evolutions graphically and examined the skin friction coefficient and local Nusselt number numerically. Muhammad et al. [5] treated the time-dependent squeezing flow of magnetohydrodynamic (MHD) Jeffrey fluid between two parallel walls where the lower one is stretched. Fluid is electrically conducted in the presence of a variable magnetic field. Through series and numerical solutions obtained, they found an excellent agreement. Unsteady MHD fluid flow in a rotational frame of reference was considered by Salman et al. [6]. The analytical solution to the studied problem was constructed using Fourier transform method. They explored the flow behaviour under the effect of magnetic and rotational parameters, and it is found that the analytical results are in good accuracy when compared with those obtained numerically. Kezzar et al. [7] studied analytically with the help of differential transform method the nonlinear problems of hydromagnetic nanofluid flow and heat transfer through converging–diverging channels. They demonstrated that the augment of Hartmann number makes disappear the reversal flow for both convergent-divergent channels, and the presence of nanoparticles within water base fluid has a direct relationship with Nusselt number enhancement. Ijaz Khan et al. [8] conducted a numerical simulation dealing with the entropy generation effectiveness in magnetohydrodynamic flow of viscous fluid by permeable rotating disk. They explored the effect of several characteristics of interest like magnetic and slip parameters, thermal and solutal buoyancy variables, Prandtl number, temperature difference parameter, radiative parameter, dimensionless reaction rate, activation energy factors, heat generation/absorption factor and Schmidt number on the behaviour of concentration, velocity and thermal fields. Ramadevi et al. [8] delivered an interesting numerical investigation of two-dimensional magnetohydrodynamic mixed convective flow of micropolar fluid past a stretching surface employing modified Fourier's heat flux model. They investigated the friction factor, couple stress and mass and thermal transport rates under the influence of flow relevant variables. The study done by Gherieb et al. [9] investigates the hydromagnetic boundary layer Falkner–Skan flow over a flat plate numerically using the Runge–Kutta method featuring shooting technique and analytically via a new modified analytical technique called improved generalized Adomian decomposition method (improved-GDM). They demonstrated that the increase of magnetic field intensity leads to an increase in fluid velocity, and consequently the backflow is prevented for both accelerated and decelerated Falkner-Skan flow. Merabet Ayeche et al. [10] investigated the two-dimensional time-dependent laminar hydromagnetic boundary-layer flow of a bio-magnetic fluid over a wedge using a micropolar fluid model with convective boundary conditions and taking into account the action of a transversely magnetic field. They interested in the effect of the wedge angle parameter β, unsteadiness parameter K, Reynolds number Re, induced magnetic field h and magnetic field parameter M on the behaviour of dimensionless velocity, temperature and micro-rotation of the bio-magnetic flow throughout the boundary layer. Mahabaleshwar et al. [11] studied the heat transfer characteristics of magnetohydrodynamic axisymmetric flow of Casson fluid analytically over a nonlinear permeable shrinking/stretching surface. They depict the effect of several physical quantities like the magnetic field, Casson parameter, mass transpiration, radiation, and Prandtl number on the evolution of the fluid velocity, temperature and skin friction coefficient. Sneha et al [12] in their investigation studied two-dimensional hydromagnetic steady incompressible Marangoni nano boundary layer flow

and heat transfer characteristics. They found that the axial velocity is affected by the viscoelastic constraint, magnetic field, and suction/injection parameters. Also, results obtained reveal that the Marangoni convection enhances the heat transfer rate; however, it diminishes with the application of magnetic energy.

Nowadays, it is well known that the heat transfer improvement in engineering systems is limited by the low base fluid thermal conductivity. In fact, a lower thermal conductivity can be considered as a major problem and consequently affects the reliability of engineering components like heat exchangers and electronic devices. To overcome this disadvantage, a novel category of fluids with excellent thermal characteristics is therefore of paramount importance to address the technological and industrial requirements. Choi [13] discovered a new nanotechnology-based fluid for heat transfer known as nanofluid (NF) in 1990 that is obtained by dispersing nano-sized solid particles (less than 100 nm) like Cu, Ag, TiO2 and CuO in a conventional base liquid. In fact, regarding the dispersed solid nanoparticles higher thermal conductivities, NF is highly considered as one of superior class of solid–liquid suspensions. After that, NFs have gained much attention and experimentally and numerically investigated by different scholars [14–24]. Belazreg et al. [25] also studied the latent of the latent heat thermal energy storage of copper nanoparticles and rubitherm (RT27) phase transition material considering four distinct stepped fin surfaces with the aim of capturing the variations of thermal entropy, temperature distribution, frictional entropy and liquid fraction in such system. This investigation uses the enthalpy-porosity technique to simulate the governing equation arising from mathematical modeling numerically. Vaidya et al. [26], in an interesting contribution, have used the Casson model to study the peristaltic blood flow of copper nanoparticles over an overlapping stenotic artery. Using stenosis approximations, they examined stream function, wall shear stress, Nusselt number, and flow resistance distribution. This investigation found that the temperature distribution increases with the rise in heat source parameter values.

Recently, several researchers have employed hybrid nanofluid (HNF) in the continuation of NF research. This new kind of nanofluid is engineered by combining a base fluid with a composite form or mixture of dissimilar suspended nanoparticles [27]. The idea of using HNFs is to further enhancement of heat transfer due to their higher thermophysical properties. The flow and heat transfer process of HNF have attracted researcher's community and intensively investigated. Experimentally, the study implemented by Esfe et al. [28] mainly concentrated on the impact of nanoparticle volume fraction (VF) on dynamic viscosity and thermal conductivity of Ag–MgO/water HNF. The presented correlations for the mentioned properties showed a good agreement with experimental data. Moreover, heat transfer properties and pressure drop of a HNF mixture containing alumina nanoparticles (Al2O3) and multi-walled carbon nanotubes (MWCNTs) were experimentally investigated by Huang et al. [29] in a chevron corrugated-plate heat exchanger. Obtained findings reveal that the HNF mixture heat transfer coefficient is slightly higher than that of the water and Al2O3/water nanofluid; however, the HNF mixture pressure drop is slightly higher than that of water and smaller than that of the Al2O3/water nanofluid. Mehrali et al. [30] experimentally analyzed the rate of entropy generation and characteristics of heat transfer of hybrid graphene-magnetite nanofluids under hydromagnetic forced laminar flow. They showed that the thermal conductivity of the considered HNF shows an enhancement of 11% and the total entropy generation rate was decremented by up to 41% in comparison with distilled water. By numerical means, studies were concentrated on heat and HNF flow analysis in several geometries. Heat transfer and hydro-magnetic flow of HNF in a rotating system among two surfaces under the effect of thermal radiation and Joule heating were investigated by Chamkha et al. [31]. This investigation revealed that the Nusselt number appears as an increasing function of radiation and injection parameters, as well as VF of the HNF. Waini et al. [32] numerically analyzed heat transfer and steady flow of Cu-Al2O3/water HNF past a permeable moving surface using bvp4c function with the
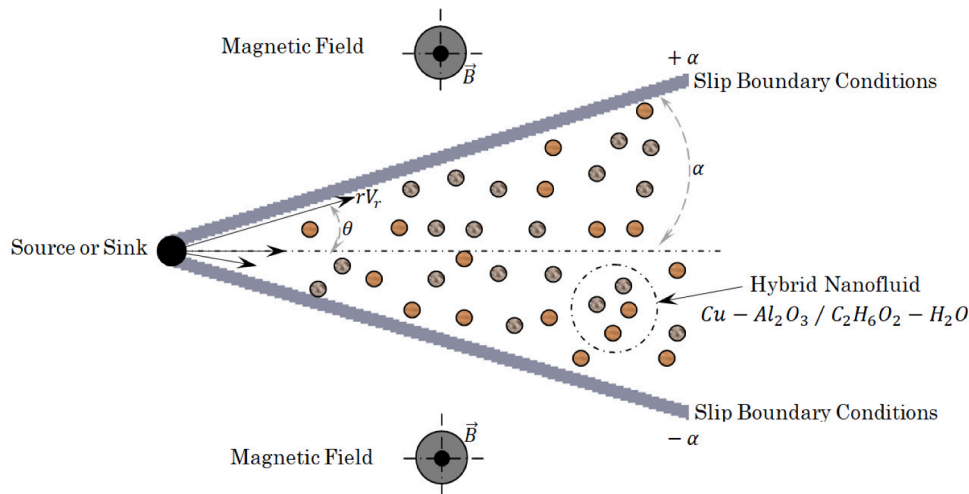
Fig. 1. Physical model for MHD Jeffery–Hamel HNF flow.

help of Matlab software. It is reported that the HNF heat transfer rate is more than the value that observed for regular nanofluid. Muhammad et al. [33] addressed a comparative study of HNF (MWCNTs + Cu + Water), nanofluid (MWCNTs + Water) and base fluid (Water). The obtained nonlinear coupled ordinary differential equation are solved with the aid of the fourth order Runge Kutta method (bvp4c) featuring the shooting technique. Animasaun et al. [34] explored the hybrid nanofluid flow on impermeable stagnant and moveable walls experiencing variable temperature. Through the conducted numerical analysis they found that minimal velocity was obtained in the case of stagnant impermeable surface; however, the minimal temperature was occured when the impermeable surface is moving. On the other hand, the minimal local skin friction coefficient was gained when the volume of used nanoparticles is sufficiently large in the case of hybrid nanofluid flow over a stagnant impermeable wall. The study undertaken by Saranya et al. [35] focuses on analyzing the quartic type homogeneous-heterogeneous reactions in ternary-hybrid nanofluid flow over the surface of a stationary/ moving flat plate. This investigation also uses the Tiwari-Das model for nano-liquid to explore the flow-thermal behaviour of the hybrid nanofluid.

It is well established that the celebrated flow driven by a line source at the the rigid plates intersection, which is known as Jeffery-Hamel flow, is of paramount importance due to its wide real practical applications like flow through rivers, reducers, nozzles and diffusers. The nonlinear governing equation, initially given by Jeffery [36] and independently by Hamel [37], was extensively treated by several researchers. For example, Rosenhead [38] gives a complete mathematical solution of the Jeffery-Hamel problem in both divergent and convergent flows. Solution obtained is expressed in terms of elliptic functions and different mathematically possible kinds of flow were explored. Fraenkel [39] for his part solved the Jeffery-Hamel equation in the case of laminar flow in channels in symmetrical geometry with marginally curved walls. In this investigation, the symmetric fluid velocity obtained is mainly dependent on two non-dimensional parameters which are the wedge semi-angle □; and the Reynolds number, R = Q/2v, based on the volume flux, Q. On the other hand, in terms of the zeros number of the solution, Fraenkel classified different zones of the (α, R)-plane. Thereafter, Millsaps and Pohlhausen [40] extended the classical Jeffery-Hamel flow to heat transfer problem. They give exact and numerical solutions for the thermal distributions in the case of steady laminar flow of a viscous incompressible fluid through convergent-divergent channels. According to the literature, many studies also deal with Jeffery-Hamel flow hydrodynamic stability. In fact, Eagles [41] interested on the stability question in divergent channel by resolving numerically the well known Orr-Sommerfeld problem. Neutral stability curves were determined in

the (k, R)-planes (in which R refers to the basic flow Reynolds number and k denotes the disturbance wave-number), and fairly low critical Reynolds numbers were observed. Sobey and Drazin [42] used experimental, numerical and analytical approaches to investigate some bifurcations and instabilities of two-dimensional channel flows. They examined Jeffery–Hamel flows and found interesting new findings about the such flows stability. Hamadiche et al. [43] interested on the Jeffery-Hamel flow temporal stability. They calculated the critical Reynolds numbers on the basis of the volume flux and axial velocity. Uribe et al. [44] also investigated the linear and temporal stability of some Jeffery-Hamel flows by using the Galerkin method. They found that the considered flows are unstable for Reynolds numbers near zero. Following previously published contributions on Jeffery-Hamel flow, Jotkar and Govindarajan [45] made a parallel-flow approximation for testing its non-modal stability in condition of low angles of convergence and divergence. They demonstrate that non-modal growth is significantly sensitive to the convergence/divergence angle in cases of high Reynolds numbers. Al-Nimr et al. [46] investigated the classical Jeffery-Hamel flow utilizing both first and second-order velocity-slip models. This investigation examines the impact of Knudsen number (Kn) on the velocity of fluid, slip magnitude at the wall, and skin friction coefficient (SFC).

According to the literature, the slip flow was investigated for various flow configurations. In fact, many researchers were interested on fluid flow behaviour and heat transfer evolution taking into account the velocity-slip boundary conditions at the wall. In a pioneering work employing direct numerical approach of the linear Boltzmann equation, Wu [47] employed an effectiveness second-order slip model that well agreed with the result obtained by Fukui and Kaneko [48]. In another interesting research-work, Zhu et al. [49] addressed the impacts of the second-order velocity slip and temperature jump boundary conditions on the magnetohydrodynamic (MHD) flow and heat transfer in the presence of solid nanoparticles. More recently, Martins Obalalu et al. [50] by using the Chebyshev collocation Method investigated numerically the effect of variable electrical conductivity on non-Darcian Casson nanofluid flow and heat transfer considering both first and second-order slip conditions. Al Jaloud et al. [51] also studied the thermal impact of bioconvection flow of cross nanofluid taking into account the second order slip condition and activation energy. They found that the nanofluid velocity decreases with interaction of first order slip parameter.

During last decades, a large number of analytical techniques, like homotopy method [52,53], variational iteration approach [54] and Adomian decomposition approach [55], were developed and successfully employed to solve ordinary and partial nonlinear differential equations. Adomian's decomposition approach was first discovered by

Georges Adomian in the 1980 s; it is considered as one of interesting techniques which gives analytical approximations and provides the solution as an infinite series with elegantly computable terms that can be easily determined. Thereafter, various modifications of the Adomian Decomposition Method (ADM) have been proposed in an attempt to enhance the efficiency of the original method. The Duan Rach Approach (DRA) [56] is considered as one of reliable modified version of the Adomian decomposition method which was principally employed for solving a large class of nonlinear boundary value problems [57–63]. In fact, this modified analytical technique will allow determining an accurate solution without using numerical methods to evaluate the undetermined coefficients and in consequence the final solution does not contain undetermined coefficients.

This study aims at modeling and simulating the dynamic behaviour of magneto-hydrodynamic HNF flow between nonparallel plane walls by considering the impact of velocity-slip boundary conditions. The obtained nonlinear ordinary differential equation governing the considered problem was treated numerically via Runge-Kutta-Fehlberg technique featuring shooting technique and analytically with the help of a new modified technique of computation called Duan-Rach Approach. In this investigation, we are mainly interested to the effect of different physical parameters of interest like Reynolds number Re, Hartmann number Ha, channel half-angle α, nanoparticles VF φ and velocity-slip boundary conditions models on SFC and velocity distribution for both diverging and converging flows. On the other hand, a comparative study was undertaken with the aim of showing accuracy and effectiveness of the adopted Duan-Rach Approach.

2. Governing equations

This investigation considers the steady magneto-hydrodynamic HNF flow via converging/diverging channels. As displayed in Fig. 1, a purely radial motion, i.e., for velocity components was assumed that can be written as: $V = V(r, \theta), V_\theta = 0$ and $V_Z = 0$. In addition, this study concerns the impacts of solid hybrid nanoparticles, magnetic field and both the first- and second-order slip models on the hydrodynamic behaviour of the considered HNF flow.

The equations for continuity and momentum in cylindrical coordinates (r, θ, z) can be written as follows:

$$\frac{1}{r}\frac{\partial}{\partial r}(rV_r) + \frac{1}{r}\frac{\partial V_\theta}{\partial \theta} + \frac{\partial V_z}{\partial z} = 0 \tag{1}$$

$$V_r\frac{\partial V_r}{\partial r} = -\frac{1}{\rho_{hnf}}\frac{\partial p}{\partial r} + \nu_{hnf}\left[\frac{\partial^2 V_r}{\partial r^2} + \frac{1}{r}\frac{\partial V_r}{\partial r} + \frac{1}{r^2}\frac{\partial^2 V_r}{\partial \theta^2} - \frac{V_r}{r^2}\right] - \frac{\sigma_{hnf}}{\rho_{hnf}r^2}\left(B^2 V_r\right) \tag{2}$$

$$0 = -\frac{1}{\rho_{hnf}}\frac{\partial p}{r\partial \theta} + \frac{2\nu_{hnf}}{r^2}\frac{\partial V_r}{\partial \theta} \tag{3}$$

The channel centerline boundary condition can be expressed as follows:

$$At\theta = 0 \rightarrow V_r = \frac{V_{max}}{r} and \partial V_r/\partial \theta = 0 \tag{4}$$
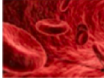
The wall velocity-slip boundary condition is as follows:

$$V_r = V_{slip} \tag{5}$$

The quantities ν_{hnf}, ρ_{hnf} and σ_{hnf} are the kinematic viscosity, density and electrical conductivity of the HNF,

The HNF properties are expressed as follows

Table 1
Solid nanoparticles shape factor.

Nanoparticles type	Shape	Shape factor
Sphere		$m = 3$
brick		$m = 3.7$
Cylinder		$m = 4.9$
Platelet		$m = 5.7$

$$\nu_{hnf} = \frac{\mu_{hnf}}{\rho_{hnf}}$$

$$\begin{cases} \mu_{hnf} = \frac{\mu_f}{(1-\varphi_1)^{2.5}(1-\varphi_2)^{2.5}} \\ \rho_{hnf} = \rho_f\left((1-\varphi_2)\left((1-\varphi_1)+\varphi_1\frac{\rho_{p1}}{\rho_f}\right)+\varphi_2.\frac{\rho_{p2}}{\rho_f}\right) \\ \frac{\sigma_{hnf}}{\sigma_f} = 1 + \frac{3(m-1)(\frac{\sigma_{p1}}{\sigma_f}-1)\varphi_1}{\left(\frac{\sigma_{p1}}{\sigma_f}+2\right)-(m-1)\varphi_1(\frac{\sigma_{p1}}{\sigma_f}-1)} \\ \quad + \frac{3(m-1)(\frac{\sigma_{p2}}{\sigma_f}-1)\varphi_2}{\left(\frac{\sigma_{p2}}{\sigma_f}+2\right)-(m-1)\varphi_2(\frac{\sigma_{p2}}{\sigma_f}-1)} \end{cases} \tag{6}$$

where m is the shape factor of the considered solid nanoparticles. Table 1 depicts different particles shapes such as sphere, brick, cylinder and platelet.

Based on the continuity equation (Eq. (1), it can be written:

$$V_r = f(\theta)/r \tag{7}$$

By employment of the following similarity transformation [19]:

$$F(\theta) = \frac{f(\theta)}{f_{max}} \tag{8}$$

where: $\eta = \frac{\theta}{\alpha}$ with:. $-1 \le \eta \le +1$

and removing pressure terms between Eqs. (2) and (3), we obtain the following dimensionless form:

$$F'' + 4\alpha^2 F' + 2Re\alpha(1-\varphi_1)^{2.5}(1-\varphi_2)^{2.5}\left[A_1 FF' - A_2 Ha\alpha^2 F'\right] = 0 \tag{9}$$

The first order wall slip boundary condition in partial differential form is given as follows:

$$f(\pm\alpha) = -\frac{2-\sigma_v}{\sigma_v}\lambda\left(\frac{\partial V_r}{\partial \theta}\right)_{\theta=\mp\alpha} \tag{10}$$

where:

σ_v: Tangential momentum accommodation coefficient (TMAC).

λ: Mean free path.

$\frac{\partial V_r}{\partial \theta}$: Velocity gradient normal to the azimuthal direction.

Using the Taylor series expansion of V_r about the wall, the second order terms slip boundary condition is thus

$$f(\pm\alpha) = -\frac{2-\sigma_v}{\sigma_v}[\lambda\left(\frac{\partial V_r}{\partial \theta}\right)_{\theta=\mp\alpha} + \lambda^2\left(\frac{\partial^2 V_r}{\partial \theta^2}\right)_{\theta=\mp\alpha}] \tag{11}$$

Table 2
Thermo-physical properties of mixture base fluid and nanoparticles.

Physical properties	$\rho (Kg/m^3)$	$\sigma (Kg/m^3)$
$C_2H_6O_2 - H_2O$	1063.8	9.75×10^{-4}
Cu	1800	2.09×10^{4}
Al_2O_3	5060	6.30×10^{7}

Using Eq. (7) and considering $\eta = \frac{\theta}{\alpha}$, the velocity gradient $\frac{\partial V_r}{\partial \theta}$ can be expressed as:

$$\frac{\partial V_r}{\partial \theta} = \frac{1}{r\alpha} F'(\eta) \tag{12}$$

In terms of F(η), the boundary conditions are:

At the channel centerline $(\eta = 0) \rightarrow F(0) = 1 \; and F'(0) = 0$ (13)

At the channel body ($\eta = \mp 1$), the velocity-slip boundary conditions (10) and (11), taking into account Eq. (12), are expressed as follows [46].

- For the first-order slip model

$$F(\pm 1) = -\frac{2 - \sigma_v}{\sigma_v} Kn \, F'(\pm 1) \tag{14}$$

- For the second order slip model

$$F(\pm 1) = -\frac{2 - \sigma_v}{\sigma_v} \left[KnF'(\pm 1) + \frac{Kn^2}{2} F''(\pm 1) \right] \tag{15}$$

where Kn is the Knudsen number which is a very important dimensionless quantity that allows characterizing the boundary conditions of a fluid flow. This number is defined as the ratio of the molecular mean free path length to a representative physical length scale and is defined as follows

$$Kn = \frac{\lambda}{r\alpha} \tag{16}$$

The local Reynolds, Re, and Hartmann, Ha, numbers given by Eq. (9) can be expressed by the following formulas:

$$R_e = \frac{rV_{max}\alpha}{\nu} = \frac{f_{max}.\alpha}{\nu} \begin{cases} V_{max} > 0, \alpha > 0 \; Divergent channel \\ V_{max} < 0, \alpha < 0 \; Convergent channel \end{cases} \tag{17}$$

where f_{max} refers to the channel centerline velocity, and, α is the channel half-angle.

$$Ha = \sqrt{\frac{\sigma_f r^2 B_0^2}{\mu_f}} \tag{18}$$

From Eq. (9), the quantities A_1 and A_2 are as follows

$$\begin{cases} A_1 = \left((1 - \varphi_2)\left((1 - \varphi_1) + \varphi_1 \frac{\rho_{p1}}{\rho_f} \right) + \varphi_2.\frac{\rho_{p2}}{\rho_f} \right) \\ \\ A_2 = 1 + \dfrac{3(m-1)(\frac{\sigma_{p1}}{\sigma_f} - 1)\varphi_1}{\left(\frac{\sigma_{p1}}{\sigma_f} + 2 \right) - (m-1)\varphi_1(\frac{\sigma_{p1}}{\sigma_f} - 1)} \\ \\ \quad + \dfrac{3(m-1)(\frac{\sigma_{p2}}{\sigma_f} - 1)\varphi_2}{\left(\frac{\sigma_{p2}}{\sigma_f} + 2 \right) - (m-1)\varphi_2(\frac{\sigma_{p2}}{\sigma_f} - 1)} \end{cases} \tag{19}$$

Table 2 displays the thermophysical properties of the pure ($H_2O - C_2H_6O_2$) base fluid and solid nanoparticles (Cu and Al_2O_3).

The SFC C_f on the basis of the wall shear stress. This definition of the quantity is as follows:

$$C_f = \frac{\tau_w}{\rho.f_{max}^2} \tag{20}$$

In which wall shear stress is denoted as

$$\tau_w = \mu_{hnf} \left(\frac{1}{r}.\frac{\partial u}{\partial \theta} \right) \Big|_{\theta = \alpha} \tag{21}$$

By applying Eq. (21) in Eq. (20), and employment of the quantities (8) and (10), the SFC is expressed as:

$$C_f^* = r^2.C_f = \frac{\frac{1}{R_e}.\frac{1}{(1 - \varphi_1)^{2.5}(1 - \varphi_2)^{2.5}}}{\left((1 - \varphi_2)\left((1 - \varphi_1) + \varphi_1 \frac{\rho_{p1}}{\rho_f} \right) + \varphi_2.\frac{\rho_{p2}}{\rho_f} \right)}.F'(1) \tag{22}$$

In simulation, it is worth to note that the behavior of SFC is mainly represented by the evolution of the quantity $F'(1)$.

3. Basic concept of DRA method

Consider the following third-order nonlinear differential equation:

$$Ly = Ny + g \tag{23}$$

Subject to the Dirichlet boundary conditions

$$y(x_1) = \alpha_0, y'(x_1) = \alpha_1, y(x_2) = \alpha_2, x_1 \neq x_2 \tag{24}$$

L is an easily invertible linear operator, N is a nonlinear operator and g is the system input.

Now, considering L^{-1} as an inverse operator that represents an n-fold integration.

In fact, applying L^{-1} to both sides of Eq. (23) yields:

$$L^{-1}Ly = L^{-1}g + L^{-1}[N + R]y \tag{25}$$

We take the inverse linear differential operator L^{-1} as

$$L^{-1} = \int_{x_0}^{\eta} \int_{x_1}^{\eta} \int_{\beta}^{\eta} d\eta d\eta d\eta \tag{26}$$

where β is a prescribed value in the specified interval. Then we have:

$$L^{-1}Ly = y(x) - y(x_0) - y'(x_1).(x - x_0) - \frac{1}{2}.y''(\beta).[(x - x_1)^2 - (x_0 - x_1)^2] \tag{27}$$

Operating with the inverse operator L^{-1} on both sides of Eq. (25) yields:

$$L^{-1}[Ny + g] = y(x) - y(x_0) - y'(x_1).(x - x_0) - \frac{1}{2}.y''(\beta).[(x - x_1)^2 - (x_0 - x_1)^2] \tag{28}$$

We differentiate Eq. (27), then let x = x_2 and solve for $y''(\beta)$, hence,

$$y''(\beta) = \frac{y'(x_2) - y'(x_1)}{x_2 - x_1} - \frac{1}{x_2 - x_1} \int_{x_1}^{x_2} \int_{\beta}^{x} [Ny + g] dxdx \tag{29}$$

Substituting Eq. (29) into Eq. (28) gives

$$\begin{aligned} y(x) = & y(x_0) - y'(x_1).(x - x_0) + \frac{1}{2}\left[(x - x_1)^2 \right. \\ & \left. - (x_0 - x_1)^2 \right] \frac{y'(x_2) - y'(x_1)}{x_2 - x_1} \\ & + L^{-1}g - \frac{1}{2}\frac{[(x - x_1)^2 - (x_0 - x_1)^2]}{x_2 - x_1} \int_{x_1}^{x_2} \int_{\beta}^{x} g dxdx \\ & - \frac{1}{2}\frac{[(x - x_1)^2 - (x_0 - x_1)^2]}{x_2 - x_1} \int_{x_1}^{x_2} \int_{\beta}^{x} Ny dxdx + L^{-1}Ny \end{aligned} \tag{30}$$

From Eq. (30), we notice that the three boundary values $y(x_0), y'(x_1)$

and $\acute{y}(x_2)$ are included and consequently the undetermined coefficient was replaced. Thereafter, the series solution and the nonlinearity are given as follows:

$$u(x) = \sum_{m=0}^{\infty} u_m(x) \tag{31}$$

$$Nu(x) = \sum_{m=0}^{\infty} A_m(x) \tag{32}$$

where:

$A_m(u_0(x), u_1(x), \cdots, u_m(x))$ are the Adomian polynomials.

According to the Duan Rach approach, the solution components are determined by the following recursion scheme:

$$y_0 = y(x_0) - \acute{y}(x_1).(x - x_0) + \frac{1}{2}\left[(x - x_1)^2 - (x_0 - x_1)^2\right]\frac{\acute{y}(x_2) - \acute{y}(x_1)}{x_2 - x_1} \\ + L^{-1}g - \frac{1}{2}\frac{\left[(x - x_1)^2 - (x_0 - x_1)^2\right]}{x_2 - x_1}\int_{x_1}^{x_2}\int_{\beta}^{x} g\,dx\,dx \tag{33}$$

$$y_{m+1} = L^{-1}A_m - \frac{1}{2}\frac{\left[(x - x_1)^2 - (x_0 - x_1)^2\right]}{x_2 - x_1}\int_{x_1}^{x_2}\int_{\beta}^{x} A_m\,dx\,dx \tag{34}$$

4. Employment Of DRA method

In this study, the nonlinear differential equation (Eq. (9) under the boundary conditions (10), (11) and (12) have been solved analytically using the modified Duan-Rach-Adomian decomposition method.

According to DRA algorithm [56], Eq. (9) can be written as:

$$\mathscr{L}F'' = -4\alpha^2 F' - 2Re\alpha(1 - \varphi_1)^{2.5}(1 - \varphi_2)^{2.5}\left[A_1 FF' + A_2 Ha\alpha^2 F'\right] \tag{35}$$

where the differential operator $\mathscr{L}$ and the inverse operator $\mathscr{L}^{-1}$ are given respectively by

$$\mathscr{L} = \frac{d^3}{d\eta^3}$$

$$L_f^{-1}(\Box) = \int_0^{\eta}\int_0^{\eta}\int_0^{\eta}(\Box)d\eta\,d\eta\,d\eta$$

Operating with $\mathscr{L}^{-1}$ on Eq. (20) and applying the boundary conditions on it, we get

$$F(\eta) - F(0) - \eta F'(0) - \frac{\eta^2}{2}F''(0) = -L^{-1}R_f(\eta) - L^{-1}N_f(\eta) \tag{36}$$

where R_f and N_f are introduced as

$$\begin{cases} R_f = (1 - \varphi_1)^{2.5}.(1 - \varphi_2)^{2.5}A_2\alpha^2(4 - Ha)\dfrac{dF(\eta)}{d\eta} \\ N_f = 2Re\alpha(1 - \varphi_1)^{2.5}.(1 - \varphi_2)^{2.5}A_1 F(\eta)\dfrac{dF(\eta)}{d\eta} \end{cases} \tag{37}$$

By putting $\eta = 1$ in Eq. (14), we obtain:

• For the first-order slip model

$$F''(0) = 2\left(-\frac{2 - \sigma_v}{\sigma_v}KnF'(1) - 1 + L_1^{-1}R_f(\eta) + L_1^{-1}N_f(\eta)\right) \tag{38}$$

• For the second order slip model

$$F''(0) = 2\left(-\frac{2 - \sigma_v}{\sigma_v}\left[KnF'(1) + \frac{Kn^2}{2}F''(1)\right] - 1 + L_1^{-1}R_f(\eta) + L_1^{-1}N_f(\eta)\right) \tag{39}$$

where

$$L_1^{-1}(\Box) = \int_0^1\int_0^{\eta}\int_0^{\eta}(\Box)d\eta\,d\eta\,d\eta \tag{40}$$

Substituting Eq. (16) into Eq. (14) yields.

• For the first-order slip model

$$F(\eta) = 1 - \eta^2 + \left(-\frac{2 - \sigma_v}{\sigma_v}KnF'(1)\eta^2 + \eta^2 L_1^{-1}R_f(\eta) + \eta^2 L_1^{-1}N_f(\eta)\right) - L^{-1}R_f(\eta) - L^{-1}N_f(\eta) \tag{41}$$

• For the second order slip model

$$F(\eta) = 1 - \eta^2 + \left(-\frac{2 - \sigma_v}{\sigma_v}\left[KnF'(1) + \frac{Kn^2}{2}F''(1)\right]\eta^2 + \eta^2 L_1^{-1}R_f(\eta) + \eta^2 L_1^{-1}N_f(\eta)\right) - L^{-1}R_f(\eta) - L^{-1}N_f(\eta) \tag{42}$$

where the first component of solution, $F_0(\eta)$, is as follows:
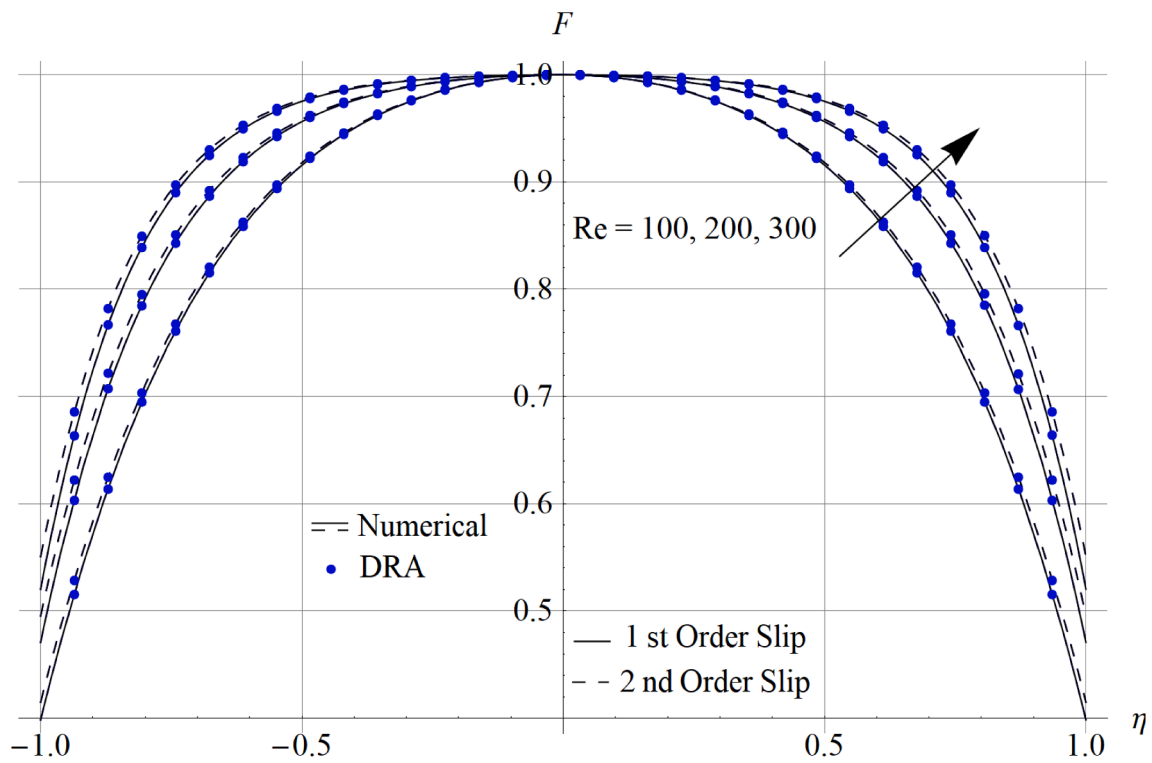
• For the first-order slip model

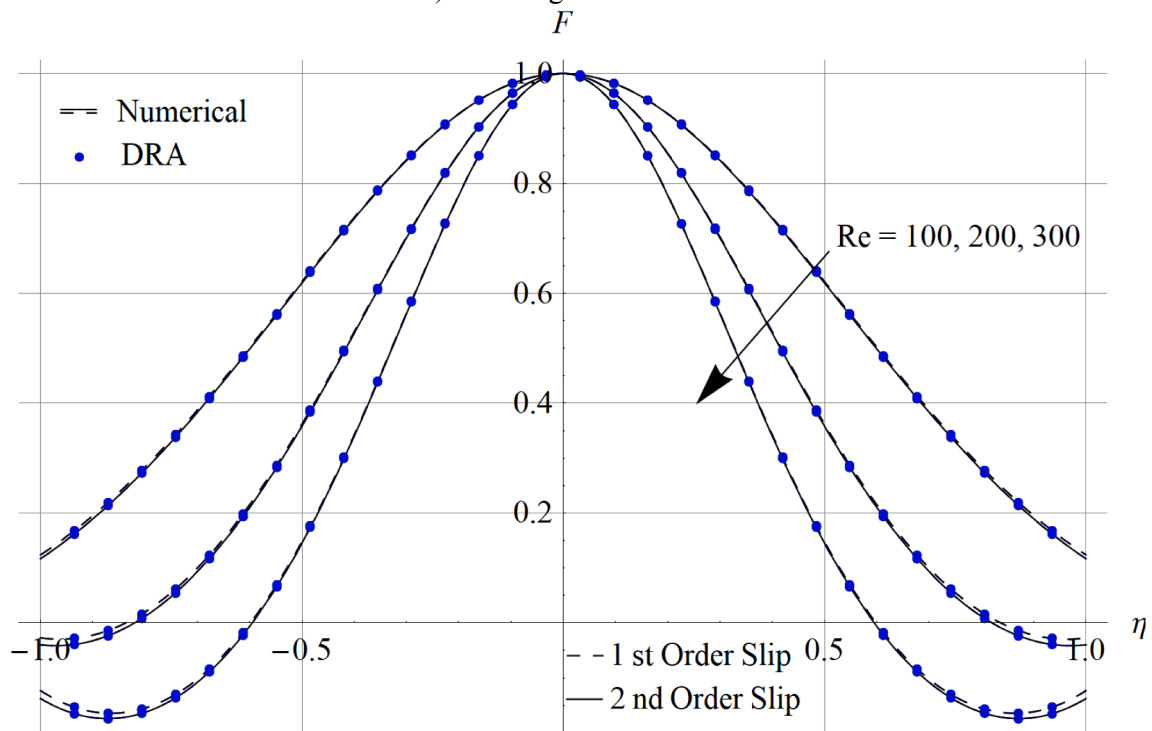$$F_0(\eta) = 1 - \eta^2 - \frac{2 - \sigma_v}{\sigma_v}KnF'(1)\eta^2 \tag{43}$$

• For the second order slip model

$$F_0(\eta) = 1 - \eta^2 - \frac{2 - \sigma_v}{\sigma_v}\left[KnF'(1) + \frac{Kn^2}{2}F''(1)\right]\eta^2 \tag{44}$$

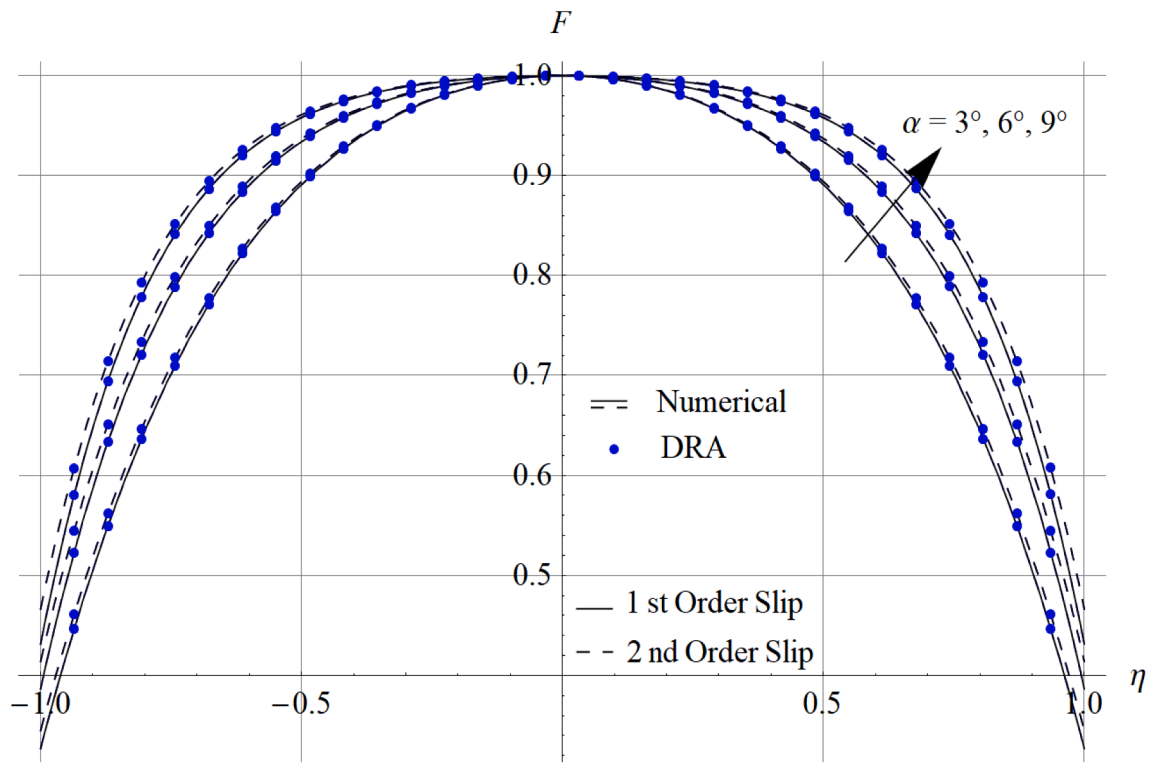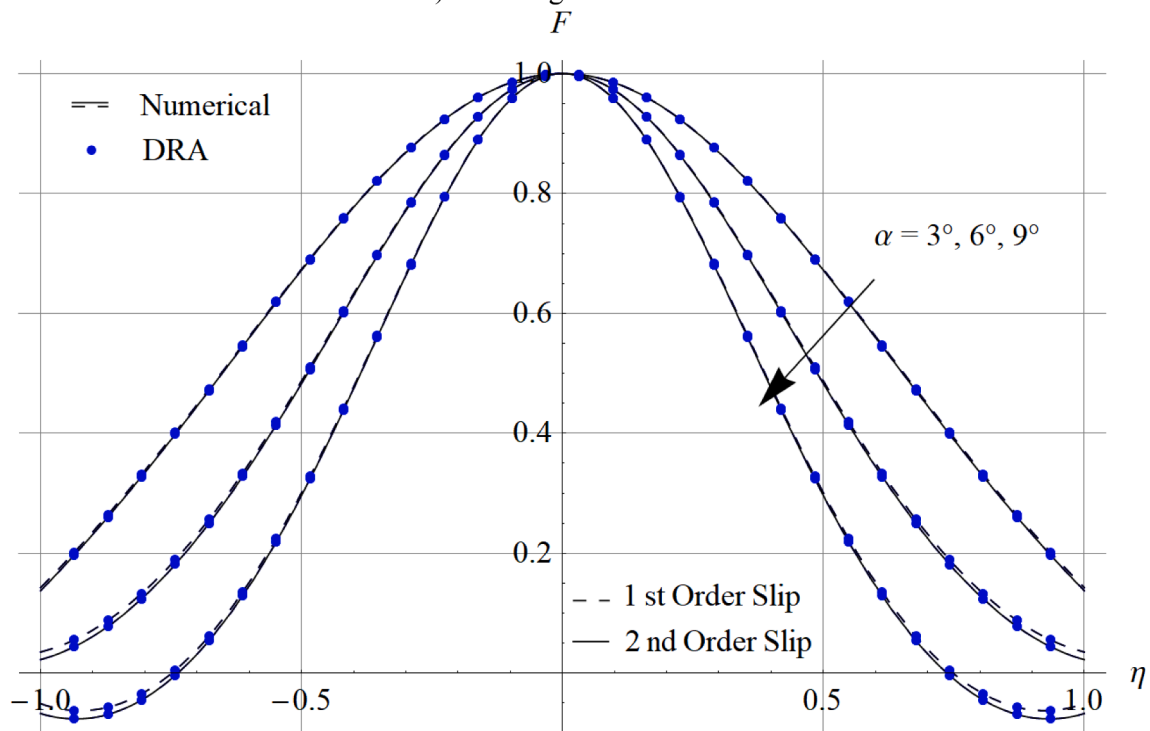Finally, the first few components of the solution determined through DRA algorithm are expressed as follows:

Fig. 2. $F(\eta)$ for different values of Reynolds number for both slip models in divergent/convergent channel when $\alpha = \pm 3^{\circ}, \varphi_{cu} = \varphi_{Al_2O_3} = 2\%, \sigma_v = 0.4, Kn = 0.05\ and\ Ha = 0$.

a). Convergent channel

b). Divergent channel

Fig. 3. $F(\eta)$ for different values of opening angle parameter for both slip models in divergent/convergent channel when. $Ha = 0, \varphi_{cu} = \varphi_{Al_2O_3} = 2.\%, \sigma_v = 0.6, Kn = 0.07 \, and \, Re = 75$
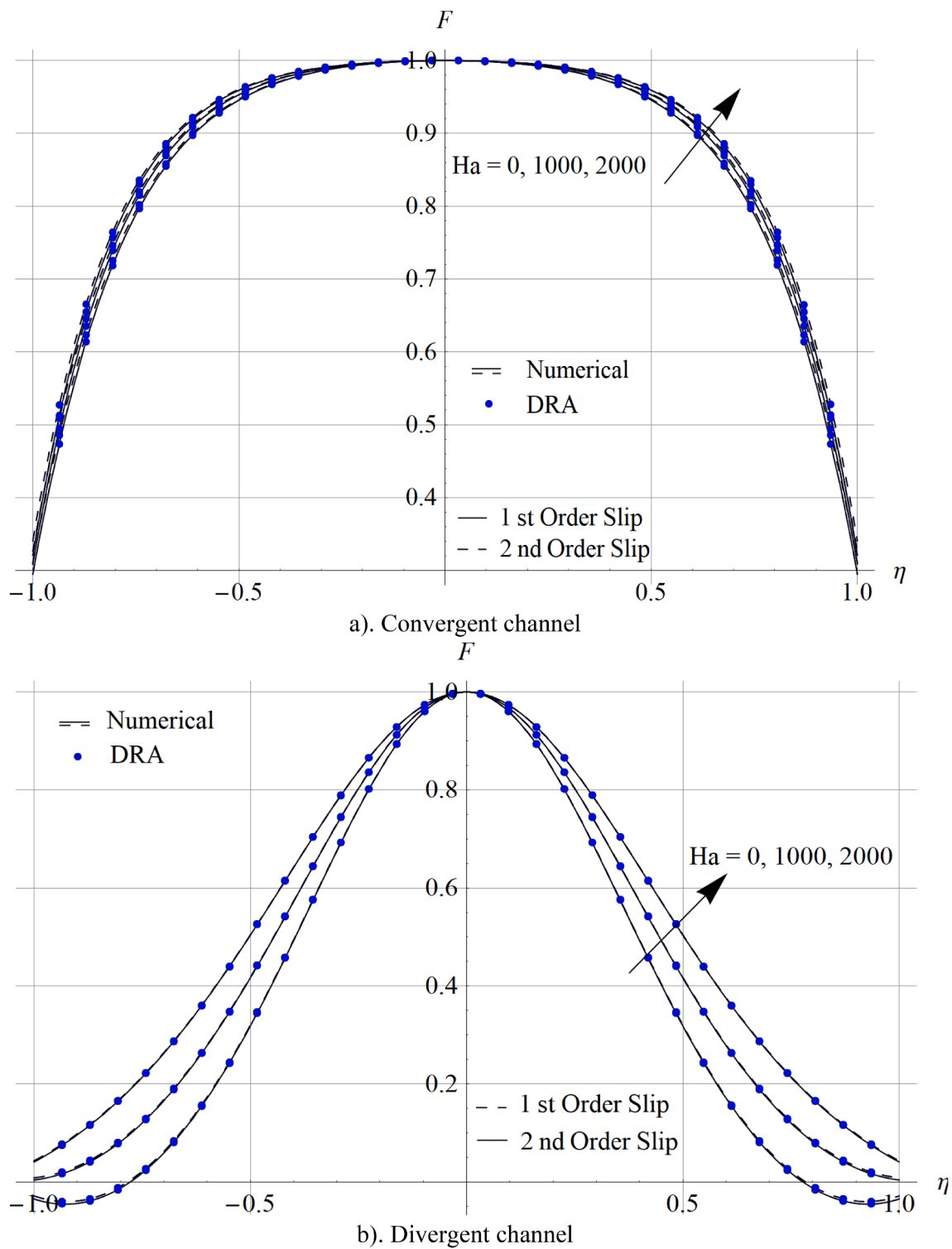
a). Convergent channel

b). Divergent channel

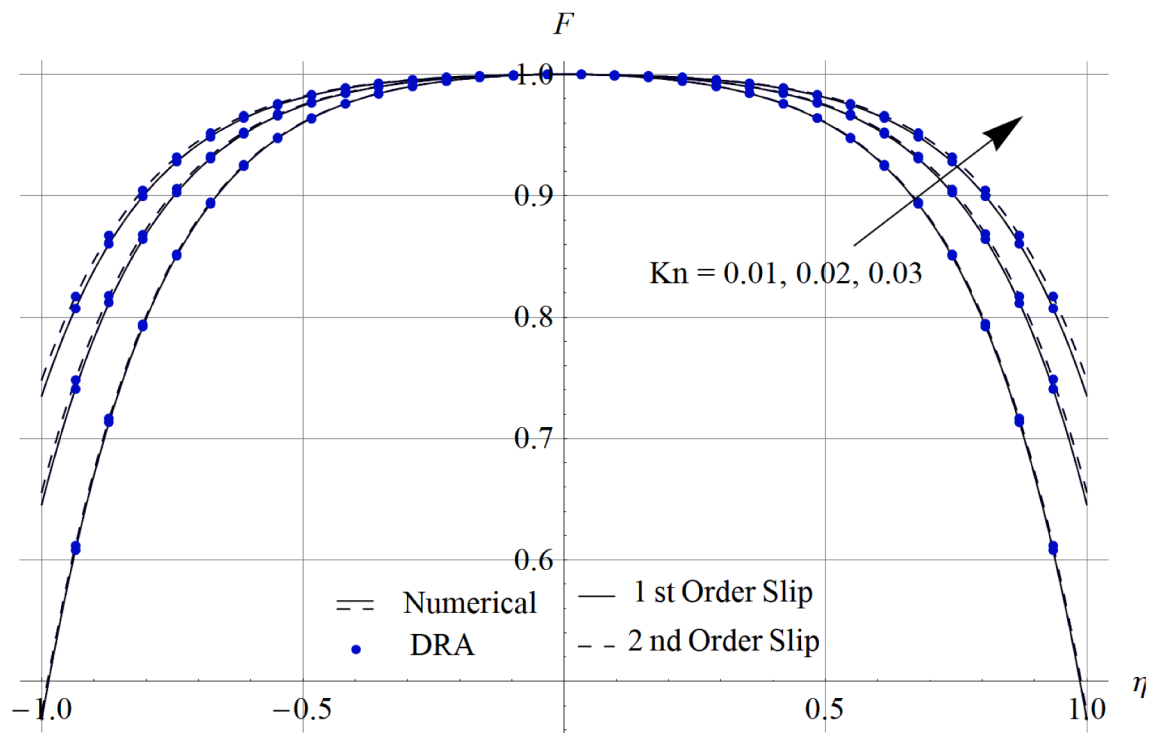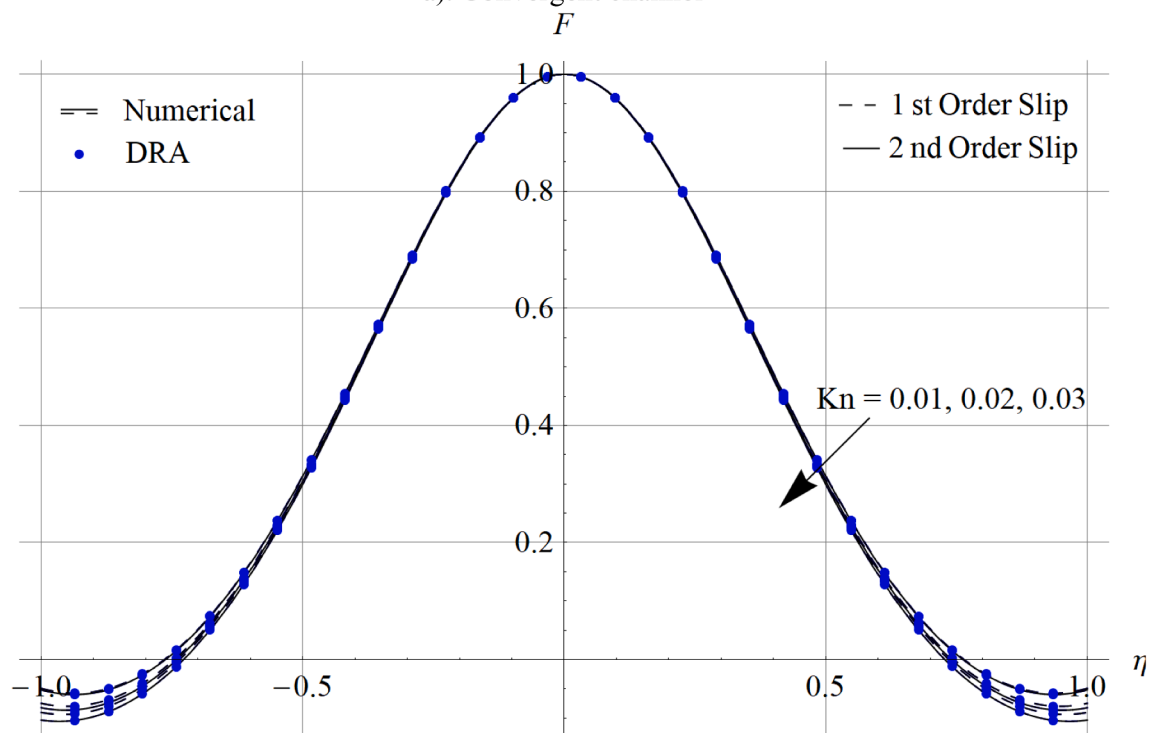**Fig. 4.** $F(\eta)$ for different values of Hartmann number for both slip models in divergent/convergent channel when. $\alpha = \pm 3°, \varphi_{cu} = \varphi_{Al_2O_3} = 2.\%, \sigma_v = 0.6, Kn = 0.04 and Re = 220$

a). Convergent channel

b). Divergent channel

Fig. 5. $F(\eta)$ for different values of Knudsen number for both slip models in divergent/convergent channel when $\alpha = \pm 3°, \varphi_{cu} = \varphi_{Al_2O_3} = 2.\%, \sigma_v = 0.6, Kn = 0.04 \, and \, Re = 220.$
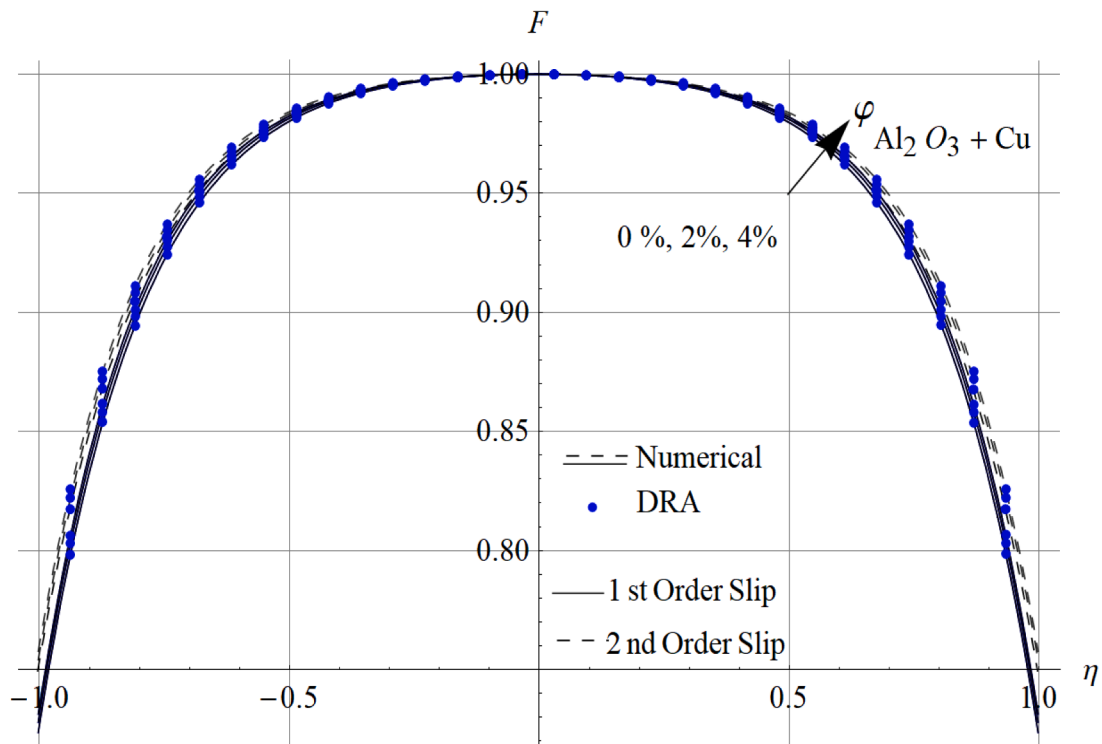
Fig. 6. $F(\eta)$ for different values of nanoparticle VF for both slip models in convergent channel when $\alpha = -3°, Ha = 0, \sigma_v = 0.2, Kn = 0.06 et Re = 240.$
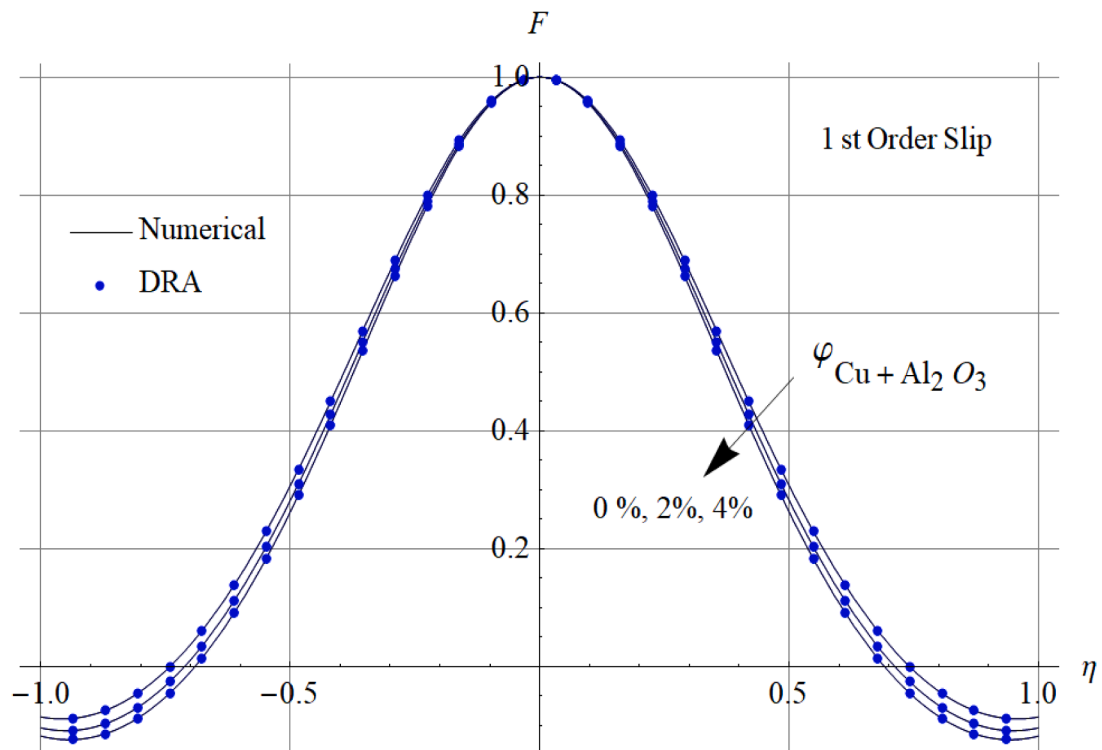

Fig. 7. $F(\eta)$ for different values of nanoparticle VF for the first-order slip model in divergent channel when. $\alpha = +3°, Ha = 0, \sigma_v = 0.2, Kn = 0.06 et Re = 240$

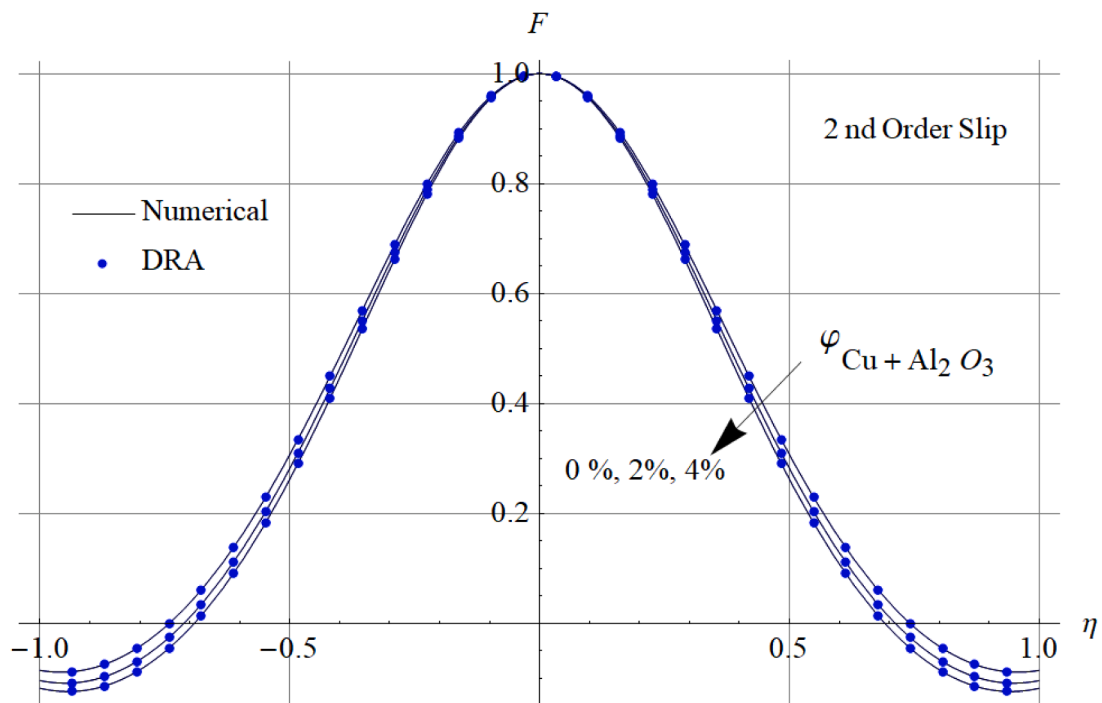**Fig. 8.** $F(\eta)$ for different values of nanoparticle VF for the second order slip model in divergent channel when. $\alpha = +3°, Ha = 0, \sigma_v = 0.2, Kn = 0.06 \, et \, Re = 240$

Fig. 9. $F(1)$ for different values of Hartmann number for both slip models in convergent channel when. $\alpha = -3°, \varphi_{cu} = \varphi_{Al_2O_3} = 1.\%, \sigma_v = 0.2, Kn = 0.06 \, and \, Re = 240$
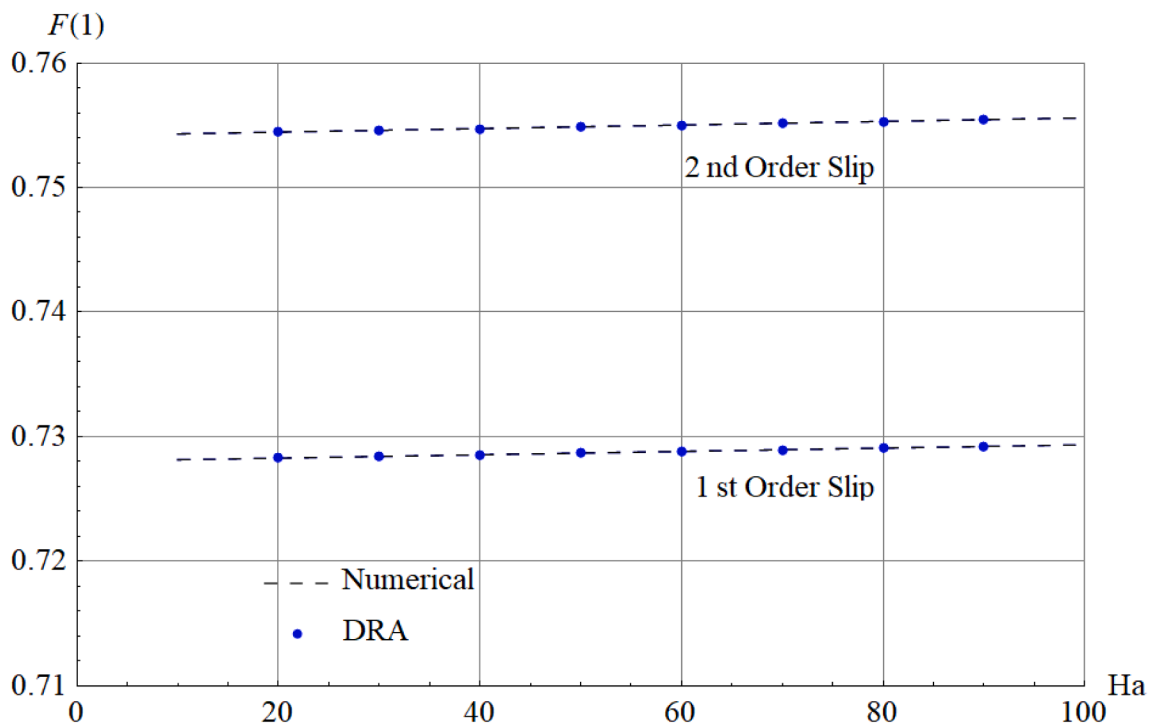
Fig. 10. $F(1)$ for different values of Hartmann number for both slip models in divergent channel when. $\alpha = +3°, \varphi_{cu} = \varphi_{Al_2O_3} = 1.\%, \sigma_v = 0.2, Kn = 0.06 \, and \, Re = 240$
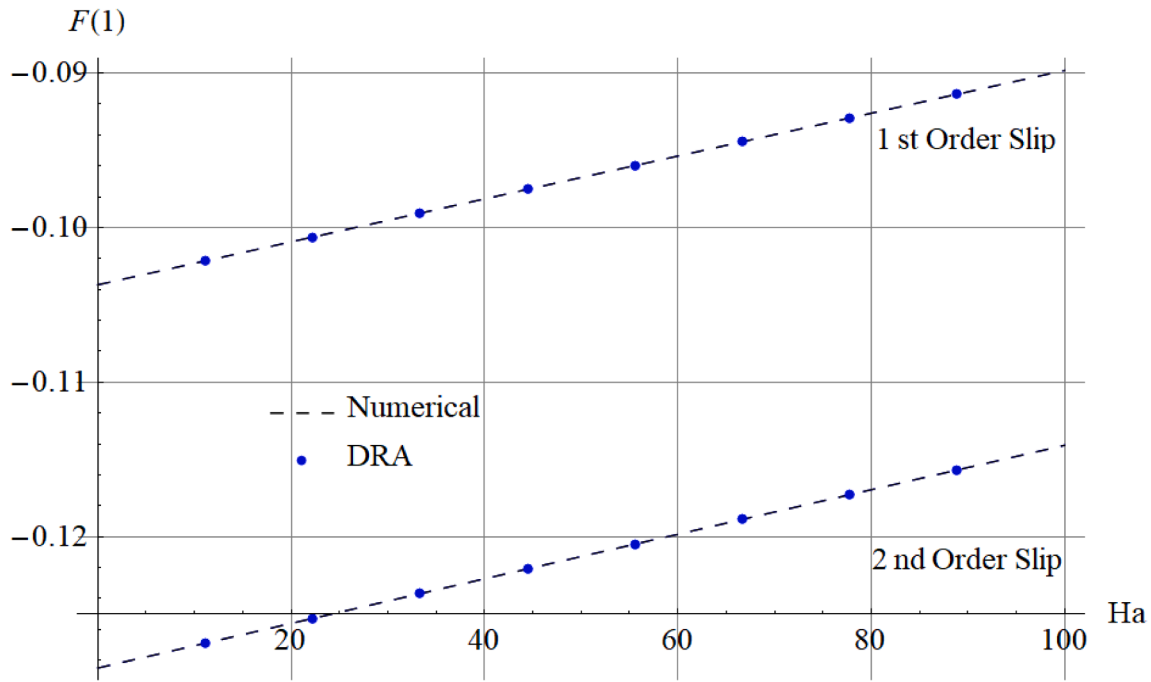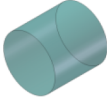
Table 3

$F(\eta)$ for different values of nanoparticles shape factor in divergent/convergent channel for both slip models when. $\alpha = \pm 3°, Ha = 1000, \varphi_{cu} = \varphi_{Al_2O_3} = 2\%, Kn = 0.04, \sigma_v = 0.6 \, and \, Re = 220$

	η	$1st^{Order Slip}$	$2nd^{Order Slip}$	$1st^{Order Slip}$	$2nd^{Order Slip}$	$1st^{Order Slip}$	$2nd^{Order Slip}$	$1st^{Order Slip}$	$2nd^{Order Slip}$
Convergent channel	0.00	1.0000	1.0000	1.0000	1.0000	1.0000	1.0000	1.0000	1.0000
	0.25	0.99218	0.99241	0.99230	0.99252	0.99248	0.99270	0.992640	0.992860
	0.50	0.95307	0.95441	0.95361	0.95496	0.95449	0.95582	0.955222	0.956553
	0.75	0.80687	0.81231	0.80824	0.8137	0.81045	0.81592	0.812299	0.817784
	1.00	0.30892	0.32694	0.30999	0.32815	0.31170	0.33011	0.313155	0.331767
Divergent channel	0.00	1.0000	1.0000	1.0000	1.0000	1.0000	1.0000	1.0000	1.0000
	0.25	0.81083	0.81048	0.81384	0.81351	0.81868	0.81837	0.822737	0.822444
	0.50	0.43385	0.43271	0.44127	0.44018	0.45322	0.45221	0.463274	0.462324
	0.75	0.13883	0.13661	0.14666	0.14453	0.15932	0.15734	0.170015	0.168158
	1.00	0.01442	0.01036	0.01734	0.01345	0.02209	0.01845	0.026121	0.022706

$$
\begin{aligned}
F_1(\eta) = &-\frac{1}{12}\alpha^2(-1+\delta)\eta^2(-4 + HaA_2(1-\varphi_1)^{2.5}(1-\varphi_2)^{2.5}) \\
&+\frac{1}{12}\alpha^2(-1+\delta)\eta^4(-4 + HaA_2(1-\varphi_1)^{2.5}(1-\varphi_2)^{2.5}) \\
&+\frac{1}{30}Re\alpha(-1+\delta)(4+\delta)\eta^2 A_1(1-\varphi_1)^{2.5}(1-\varphi_2)^{2.5} \\
&-\frac{1}{15}Re\alpha(-1+\delta)(\frac{5\eta^4}{2}+\frac{1}{2}(-1+\delta)\eta^6)A_1(1-\varphi_1)^{2.5}(1-\varphi_2)^{2.5}
\end{aligned}
$$

(45)
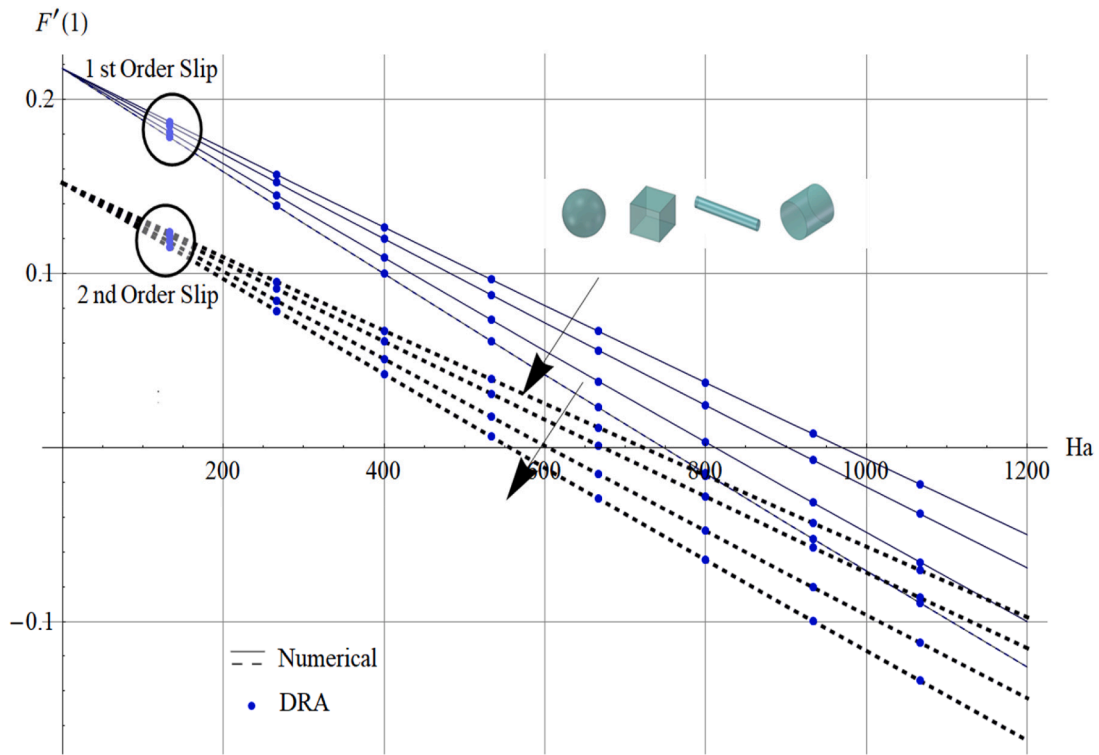
Fig. 11. SFC for different values of Hartmann number and shape factors for both slip models in divergent channel when. $\alpha = 3^{\circ}, \varphi_{cu} = \varphi_{Al_2O_3} = 2\%, \sigma_v = 0.2, Kn = 0.06 \, et \, Re = 240$
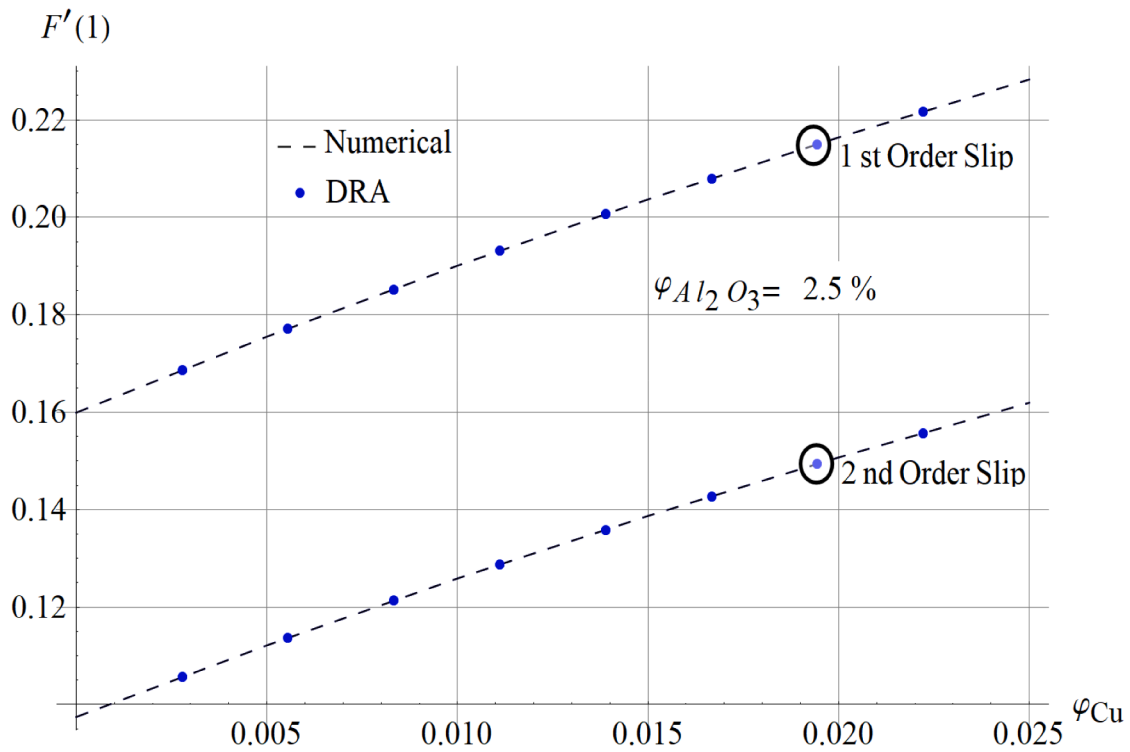
Fig. 12. SFC for different values of nanoparticle VF φ_{Cu} for both slip models in divergent channel when $\alpha = 3^{\circ}, Ha = 0, \varphi_{Al_2O_3} = 2.5\%, \sigma_v = 0.2, Kn = 0.06 \, et \, Re = 240$.
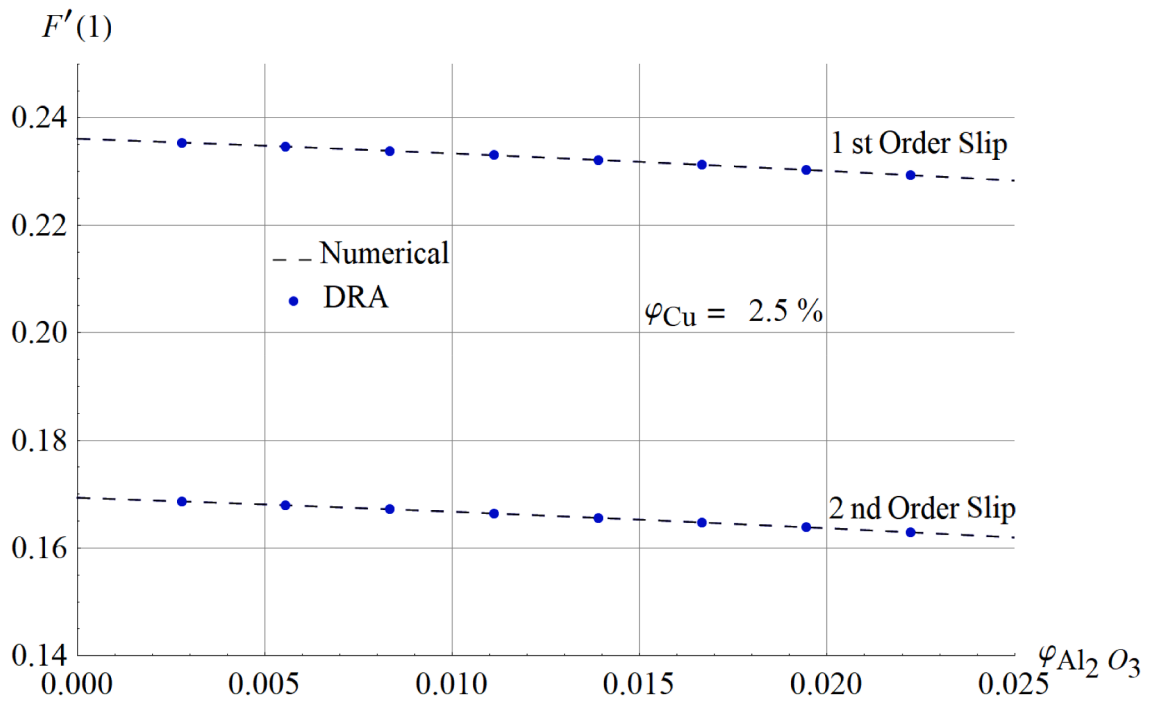
Fig. 13. SFC for different values of nanoparticle VF $\varphi_{Al_2O_3}$ for both slip models in divergent channel when $\alpha = 3^\circ, Ha = 0, \varphi_{Cu} = 2.5\%, \sigma_v = 0.2, Kn = 0.06 \, et \, Re = 240$.

Fig. 14. SFC for different values of Knudsen number and nature of nanoparticles for both slip models in divergent channel when. $\alpha = 3^\circ, Ha = 0, \varphi_{cu} = \varphi_{Al_2O_3} = 2\%, \sigma_v = 0.2 \, and \, Re = 220$

Fig. 15. SFC for different values of Knudsen number and nature of base fluid for both slip models in divergent channel when $\alpha = 3^\circ, Ha = 0, \varphi_{cu} = \varphi_{Al_2O_3} = 2\%$, $\sigma_v = 0.2$ and $Re = 220$.
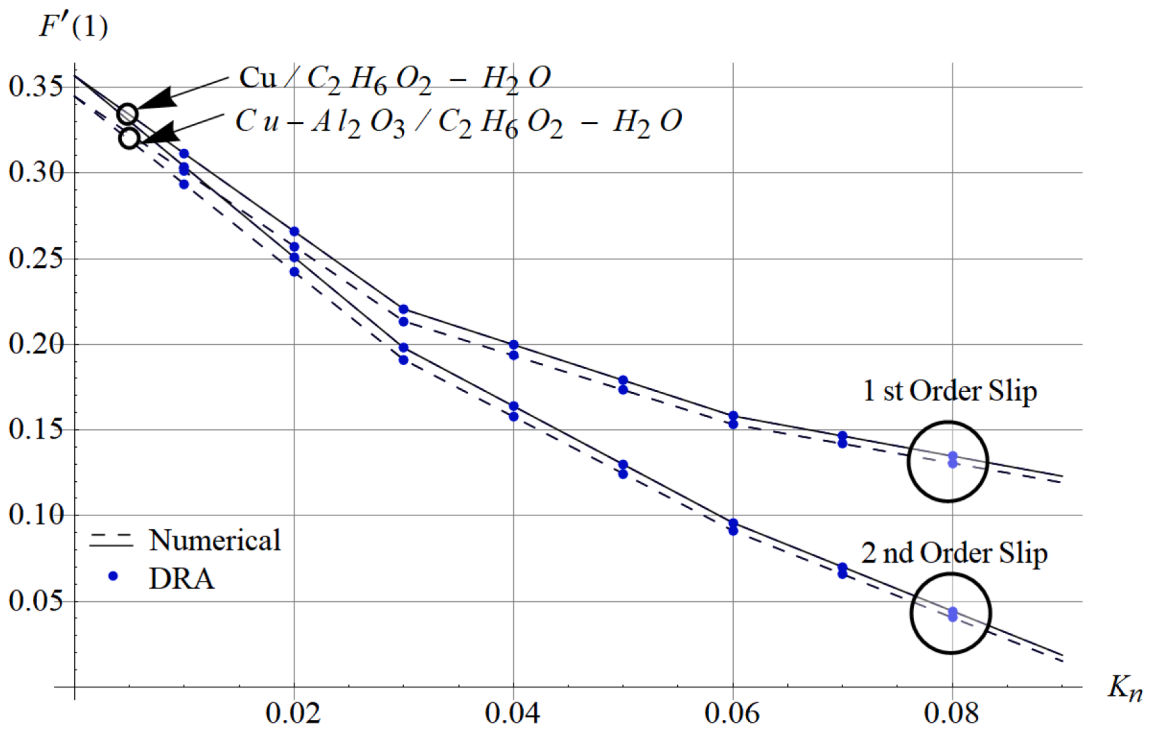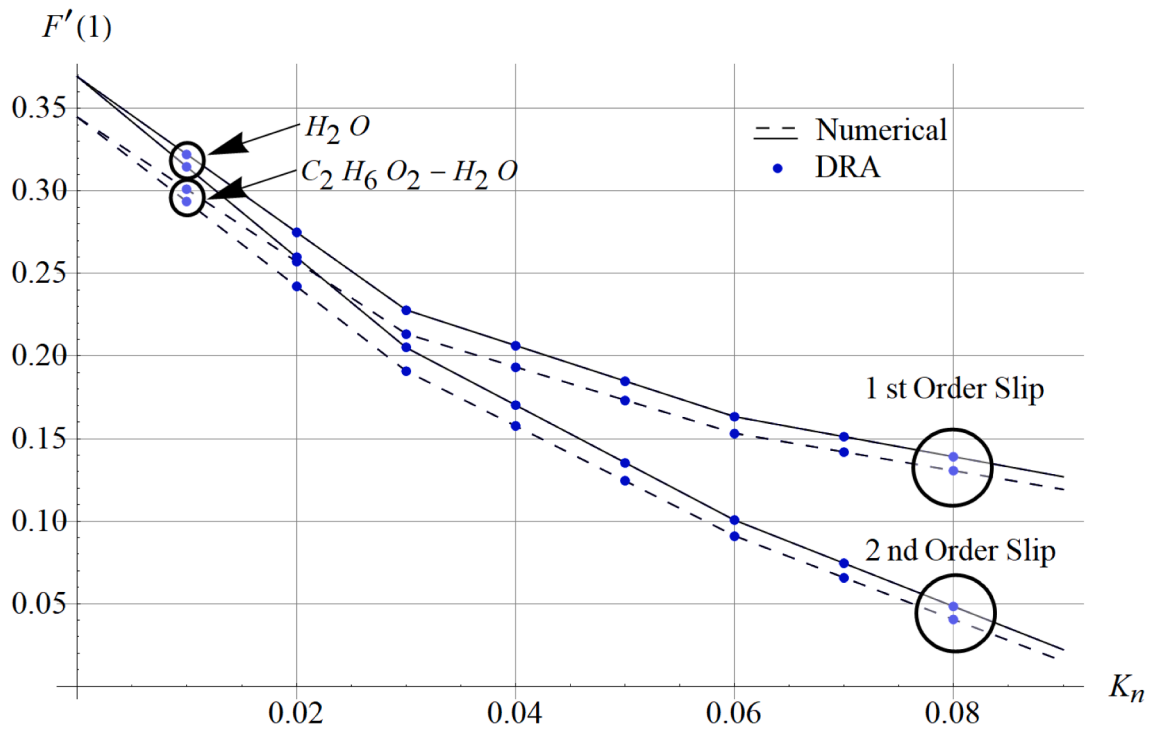
$$
\begin{aligned}
F_2(\eta) = \frac{1}{30}\alpha^3(-1+\delta)\eta^4(\text{Re}A_1((-1.33 + 0.66\eta^2 - 0.0714\eta^4 \\
+\delta(-0.33 + 0.071\eta^4))(1.-1.\varphi_1)^{2.5}(1.-1.\varphi_2)^{2.5} + \text{Ha}(0.33 - 0.16\eta^2 \\
+0.017\eta^4 + \delta(0.083 - 0.017\eta^4))A_2(1.-1.\varphi_1)^{5.}(1.-1.\varphi_2)^{5.}) + \alpha(-3.33 \\
+1.33\eta^2 + \text{Ha}(1.66 - 0.66\eta^2)A_2(1.-1.\varphi_1)^{2.5}(1.-1.\varphi_2)^{2.5} + \text{Ha}^2(-0.20 \\
+0.083\eta^2)A_2^2(1.-1.\varphi_1)^{5.}(1.-1.\varphi_2)^{5.})) - \frac{1}{30}\alpha^3(-1+\delta)\eta^2(-1.99\alpha \\
+(\text{Re}(-0.73 - 0.26\delta)A_1 + 0.99\text{Ha}\alpha A_2)(1.-1.\varphi_1)^{2.5}(1.-1.\varphi_2)^{2.5} \\
+\text{Ha}A_2(\text{Re}(0.18 + 0.06\delta)A_1 - 0.124\text{Ha}\alpha A_2)(1.-1.\varphi_1)^{5.}(1.-1.\varphi_2)^{5.}) \\
-\frac{1}{15}\text{Re}\alpha^2(-1+\delta)\eta^4A_1(1-\varphi_1)^{2.5}(\alpha(0.83 - 0.66\eta^2 + 0.33\delta\eta^2 + 0.17\eta^4 - 0.17\delta\eta^4 + \text{Ha}(-0.20 \\
+(0.16 - 0.08\delta)\eta^2 + (-0.04 + 0.044\delta)\eta^4)A_2(1.-1.\varphi_1)^{2.5}(1.-1.\varphi_2)^{2.5} + \text{Re}(0.33 - 0.3\eta^2 + 0.1\eta^4 - 0.011\eta^6 + \delta^2(0.03\eta^2 - 0.011\eta^6) + \delta(0.08 \\
+0.1\eta^2 - 0.1\eta^4 + 0.02\eta^6))A_1(1.-1.\varphi_1)^{2.5}(1.-1.\varphi_2)^{2.5})(1-\varphi_2)^{2.5} \\
+\frac{1}{15}\text{Re}\alpha^2(-1+\delta)\eta^2A_1(1-\varphi_1)^{2.5}(\alpha(0.34 + 0.15\delta) + (\text{Re}(0.12 + 0.09\delta + 0.022\delta^2)A_1 + \text{Ha}\alpha(-0.08 - 0.03\delta)A_2)(1.-1.\varphi_1)^{2.5}(1.-1.\varphi_2)^{2.5})(1-\varphi_2)^{2.5}
\end{aligned}
\tag{46}
$$

Table 4
The comparison between DRA results and numerical solution for $F(\eta)$ in divergent channel for both slip models when. $Re = 10, Ha = 5, \varphi_{cu} = \varphi_{Al_2O_3} = 1\%, Kn = 0.01$, $\sigma_v = 0.2$ et $\alpha = +2^\circ$.

	η	Numerical RKF-45	DRA Method	Error
	0	1	1	0
The first-order slip model	0.2	0.9642171544996551	0.9642171620393865	7.53×10^{-9}
	0.4	0.8578724562523676	0.8578724681953145	1.19×10^{-8}
	0.6	0.6837308130254167	0.6837308223408145	9.31×10^{-9}
	0.8	0.44561312617128185	0.4456131335620474	7.39×10^{-9}
	1	0.1473207704772301	0.14732077791531234	7.43×10^{-9}
The second order slip model	η	Numerical RKF-45	DRA Method	Error
	0	1	1	0
	0.2	0.9642399630606179	0.9642399706004503	7.53×10^{-9}
	0.4	0.8579630743085713	0.8579630862498684	1.19×10^{-8}
	0.6	0.6839326880956572	0.6839326974119031	9.31×10^{-9}
	0.8	0.44596805971584447	0.4459680671055834	7.38×10^{-9}
	1	0.14787012343996667	0.14787013087200618	7.43×10^{-9}

Table 5

The comparison between DRA results and numerical solution for $F(\eta)$ in convergent channel for both slip models when. $Re = 10, Ha = 5, \varphi_{cu} = \varphi_{Al_2O_3} = 1\%, Kn = 0.01, \sigma_v = 0.2$ et $\alpha = -2°$.

	η	Numerical RKF-45	DRA Method	Error
	0	0	0	0
The first-order slip model	0.2	0.9678984546404373	0.9678984564963492	1.85×10^{-9}
	0.4	0.8706815599995792	0.8706815555926373	4.40×10^{-9}
	0.6	0.7057723949657546	0.705772383390034	1.15×10^{-8}
	0.8	0.46943790096568927	0.46943788002441694	2.09×10^{-8}
	1	0.15772526992991098	0.15772524112863218	2.88×10^{-8}
The second order slip model	η	Numerical RKF-45	DRA Method	Error
	0	0	0	0
	0.2	0.9679270979799004	0.9679270998398076	1.85×10^{-9}
	0.4	0.8707969203040761	0.870796915908161	4.39×10^{-9}
	0.6	0.7060345970586877	0.7060345854883355	1.15×10^{-8}
	0.8	0.46990938612409383	0.46990938612409383	2.09×10^{-8}
	1	0.15846939493860362	0.15846936615061477	2.87×10^{-8}

where δ is a constant which mainly depends on the slip model. In fact, according to the Eqs. (28) and (29), δ is given by:

For the first-order slip model:

$$\delta = -\frac{2-\sigma_v}{\sigma_v} Kn F'(\pm 1) \tag{47}$$

For the first-order slip model:

$$\delta = -\frac{2-\sigma_v}{\sigma_v}\left[KnF'(\pm 1)+\frac{Kn^2}{2}F''(\pm 1)\right] \tag{48}$$

5. Results and discussions

This research-work investigates analytically via Duan-Rach modified Adomian decomposition method the nonlinear problem of HNF flow between nonparallel plane walls. In fact, a particular attention is dedicated to the effects of various physical parameters like solid hybrid nanoparticles, magnetic field and both the first- and second-order slip models on the hydrodynamic behaviour and skin friction coefficient. This investigation also uses numerical Fehlberg-Runge-Kutta solution as a guide to visualize the effectiveness of the analytical DRA method adopted.

5.1. Hydrodynamic behaviour

Fig. 2 displays the impact of Reynolds number on the HNF velocity through divergent/convergent channels for both velocity-slip boundary conditions models when $\alpha = \pm 3°$, $\varphi_{cu} = \varphi_{Al_2O_3} = 2\%$, $\sigma_v = 0.4$, $Kn = 0.05$ and $Ha = 0$. From Fig. 2.a, for convergent flow, it is noted a symmetric HNF velocity profiles against $\eta = 0$. Furthermore, an increment in the values of Reynolds number induces an increase in the nanofluid velocity leading to the flatter profile at the channel centerline and consequently a reduction can be occurred in the thickness of momentum

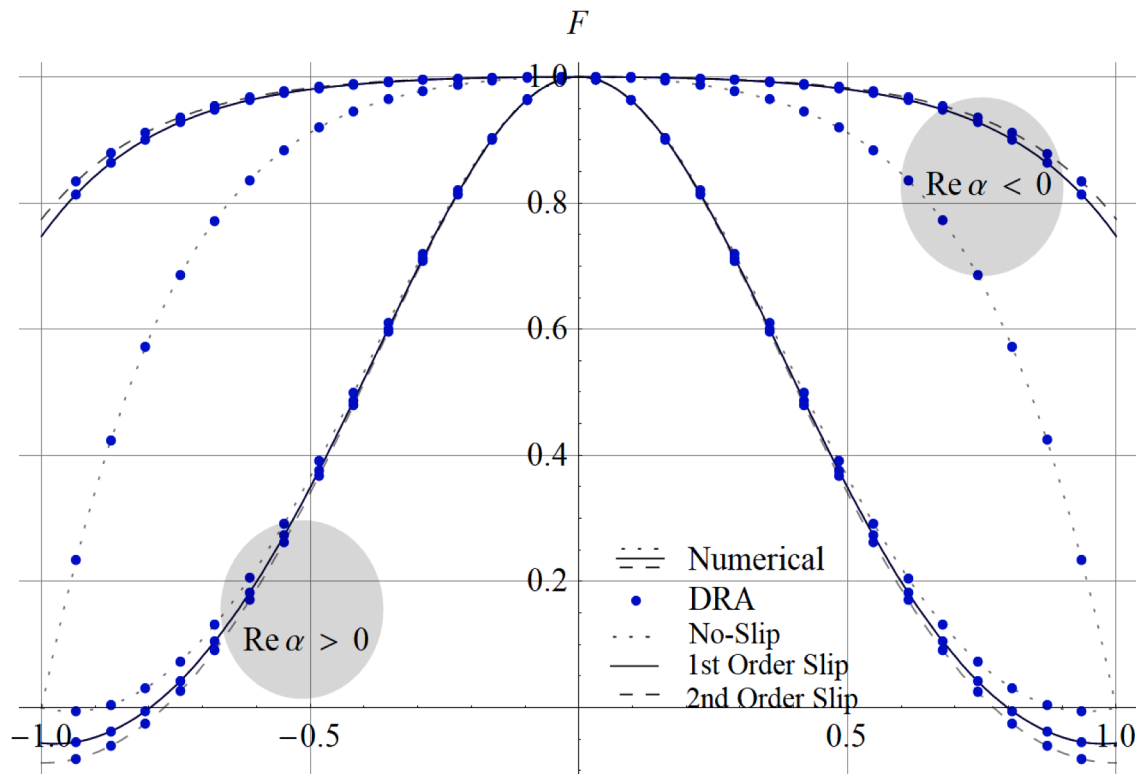
Fig. 16. Comparison between DRA method and numerical RKF-45 technique for $F(\eta)$ for both slip models in divergent/convergent when. $Re = 222, Ha = 0, \varphi_{cu} = \varphi_{Al_2O_3} = 0\%, Kn = 0.07, \sigma_v = 0.2$ et $\alpha = \pm 3°$.
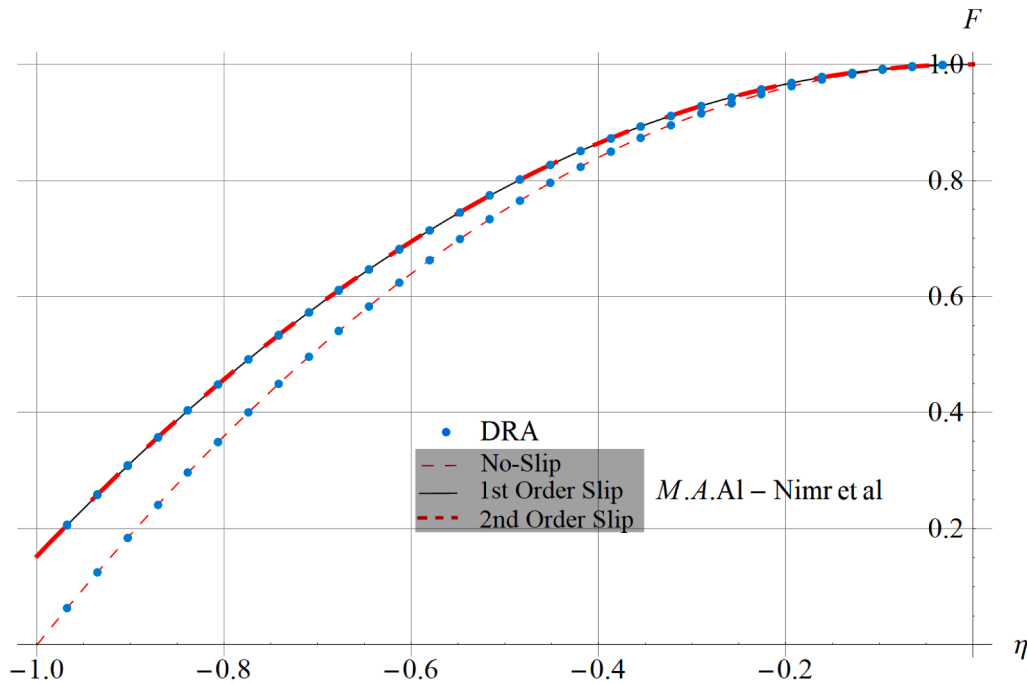
Fig. 17. Comparison between DRA data and results obtained by Al-Nimr et al. [46] for $F(\eta)$ for both slip models when. $Re\,\alpha = 0$.
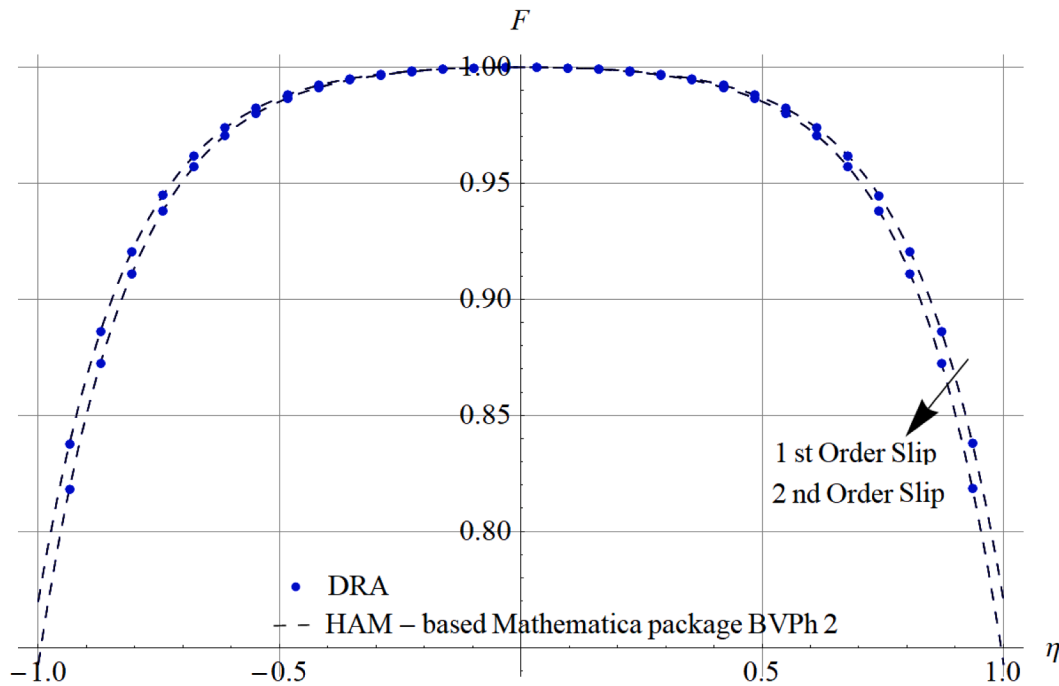

Fig. 18. Comparison between DRA data and and HAM-based mathematica package BVPh2 for both slip models in convergent channel when. $\alpha = -3°, \varphi_{cu} = \varphi_{Al_2O_3} = 1.\%, \sigma_v = 0.2, Kn = 0.06, Re = 240\,and\,Ha = 100$

boundary layer for both velocity-slip boundary conditions considered. In this situation, it is clear that the backflow is entirely excluded. From Fig. 2.a, it is also seen that the slip velocity at the wall level is higher when the Reynolds number augment. In fact, it can be highly stated that the slip starts to increase as Reynolds number increase. However, as depicted in Fig. 2.b, in the case of diverging channel, we observe that the HNF velocity appears as a decreasing function with the increase of Reynolds number where the volume flux is concentrated at the level of channel centerline with smaller gradients near the walls. In fact, this velocity decrease makes increase momentum boundary layer thickness

for both velocity-slip boundary conditions adopted. From Fig. 2.b, it is clear that the slip velocity at the wall is smaller and results obtained show that the slip decreases with the augment of Reynolds number. In the case of divergent channel, the separation and backflow phenomena are highly noticed when the Reynolds number exceeds a certain critical value.

In order to visualize the effect of channel half-angle, α, on the evolution of HNF velocity in converging/diverging channels, Fig. 3 is generated with the following data:$Ha = 0, \varphi_{cu} = \varphi_{Al_2O_3} = 2\%, \sigma_v = 0.6,$ $Kn = 0.07\,and\,Re = 75$. In fact, as drawn in Fig. 3, the behaviour of the

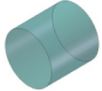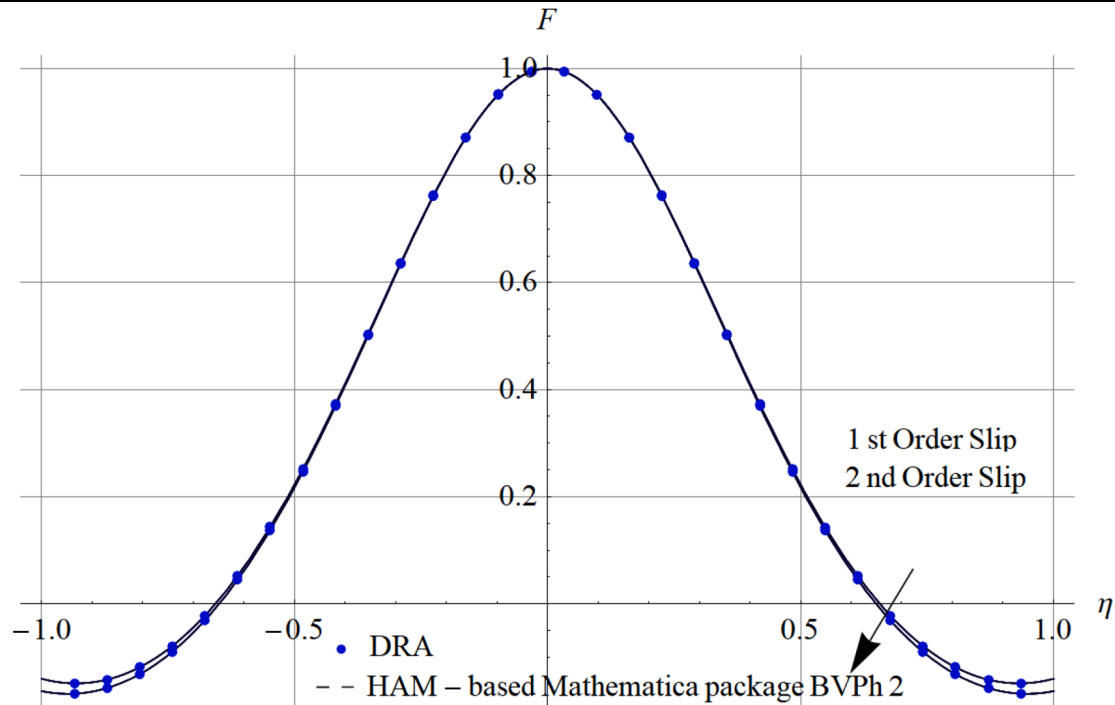|	η	1st Order Slip	2nd Order Slip	1st Order Slip	2nd Order Slip	1st Order Slip	2nd Order Slip	1st Order Slip	2nd Order Slip
Convergent channel	0.00	1.0000	1.0000	1.0000	1.0000	1.0000	1.0000	1.0000	1.0000
	0.25	0.99218	0.99241	0.99230	0.99252	0.99248	0.99270	0.992640	0.992860
	0.50	0.95307	0.95441	0.95361	0.95496	0.95449	0.95582	0.955222	0.956553
	0.75	0.80687	0.81231	0.80824	0.8137	0.81045	0.81592	0.812299	0.817784
	1.00	0.30892	0.32694	0.30999	0.32815	0.31170	0.33011	0.313155	0.331767
Divergent channel	0.00	1.0000	1.0000	1.0000	1.0000	1.0000	1.0000	1.0000	1.0000
	0.25	0.81083	0.81048	0.81384	0.81351	0.81868	0.81837	0.822737	0.822444
	0.50	0.43385	0.43271	0.44127	0.44018	0.45322	0.45221	0.463274	0.462324
	0.75	0.13883	0.13661	0.14666	0.14453	0.15932	0.15734	0.170015	0.168158
	1.00	0.01442	0.01036	0.01734	0.01345	0.02209	0.01845	0.026121	0.022706

Fig. 19. Comparison between DRA data and and HAM-based mathematica package BVPh2 for both slip models in divergent channel when. $\alpha = +3^{\circ}, \varphi_{cu} = \varphi_{Al_2O_3} = 1.\%, \sigma_v = 0.2, Kn = 0.06, Re = 240 \, and \, Ha = 100$

HNF velocity is depicted to be similar to that observed in Fig. 2 for both velocity-slip boundary conditions. In the case of converging channel (Fig. 3-a), results obtained reveal that the augment of α makes grow the favourable pressure gradient. However, in diverging channel, as depicted in Fig. 3-b, it is highly noticed that the rise in the magnitude of α promotes the apparition of reversal flow when the adverse pressure gradient is large enough.

Fig. 4 displays the effect of Hartman number, Ha, on the nanofluid velocity in convergent-divergent channels when: $\alpha = \pm 3^{\circ}, \varphi_{cu} = \varphi_{Al_2O_3} = 2\%, \sigma_v = 0.6, Kn = 0.04$ and $Re = 220$. HNF velocity profiles resulting from first and second-order velocity-slip models appear as an increasing function with the augment in the Hartmann number magnitude. In fact, this increase reduces the momentum boundary layer thickness. As witnessed this figure, it is well clear that the magnetic field has a stabilizing effect on the HNF flow behaviour. In fact, the applied magnetic field produces a well-known Lorentz force that opposes to the flow direction,

and therefore the backflow phenomenon is entirely precluded in the entire channel. Furthermore, results obtained also show that the velocity-slip at the body of channel augments with the increment of Hartmann number for both converging and diverging flows.

Knudsen number influence on the nanofluid velocity through converging/diverging channels is displayed in Fig. 5 for both considered slip models when $\alpha = \pm 3^{\circ}, \varphi_{cu} = \varphi_{Al_2O_3} = 2.\%, \sigma_v = 0.6, Kn = 0.04$ and $Re = 220$. From Fig. 5.a, in the case of convergent channel, it can be seen that the slip at the wall increases with the increase of Knudsen number, Kn for both considered slip models. In the convergent channel, it is highly stated that the backflow phenomenon is entirely vanished. On the other hand, as visualized by Fig. 5.b in the case of divergent channel, we notice that increasing Kn number makes nanofluid velocity to slowly decrease and momentum boundary layer thickness to slowly augment. Also, as the Knudsen number increases the thickness of momentum boundary layer decreases for the two considered slip models of

Table 6

Order of approximation of DRA solution for $F''(0)$ in divergent/convergent channel when. $\alpha = \pm 3°, Ha = 0, \varphi_{cu} = \varphi_{Al_2O_3} = 2\%, Kn = 0.05, \sigma_v = 0.4$ and $Re = 100$

Order approximation	$F''(0)$ in divergent channel	$F''(0)$ in convergent channel
5 th- order approximation	−3.7507596372	−0.5434355318
7 th- order approximation	−3.7484222773	−0.5411937259
9 th- order approximation	−3.7488909026	−0.5410981683
15 th- order approximation	−3.7488509679	−0.5411264397
21 th- order approximation	−3.7488583534	−0.5411326294
27 th- order approximation	−3.7488583363	−0.5411320154
Numerical	−3.7488583369	−0.5411320119

boundary conditions. Consequently, for large values of Reynolds number Re = 220, it is highly noted that the reversal flow appears for small amount of Knudsen number (i.e. Kn = 0.01) and disappear with the rise of Knudsen number.

The influence of nanoparticles VF $\left(\varphi_{cu} + \varphi_{Al_2O_3}\right)$ mixture on the HNF velocity through convergent/divergent channels is reported in Figs. 6, 7 and 8 for both velocity-slip models when $\alpha = \pm 3°, Ha = 0, \sigma_v = 0.2$, $Kn = 0.06$ and $Re = 240$. As drawn in Fig. 6 in the case of convergent flow, it can be seen for both first and second-order velocity-slip models that the nanofluid velocity increases with the rise of nanoparticle VF and consequently the backflow phenomenon is precluded. But as illustrated in Figs. 7 and 8 for the condition of divergent flow, it is observed that the velocity slip at the wall decreases with the increase of nanoparticle VF. Also, it is clearly seen that the nanofluid velocity appears as a decrementing function of the mixture nanoparticle VF and consequently the flow separation may occur for both first and second order velocity-slip boundary conditions.

Fig. 9 displays the impact of Hartmann number on the evolution of hybrid nanofluid velocity at the level of upper wall of convergent channel for both first and second-order velocity-slip boundary conditions studied. In fact, we notice a little variation of hybrid nanofluid velocity with the rise in the magnitude of Hartmann number for both slip conditions. However, as depicted in Fig. 10, in the case of divergent channel, we notice that the HNF velocity at the wall rises with the augment of Hartmann number which mainly leads to the reversal flow disappeared. On the other hand, it is highly recognized that the second-order velocity slip condition is very different from the first-order velocity slip because two slip parameters can effectively regulate the boundary layer development. When comparing the considered velocity-slip boundary conditions, as drawn in Figs. 9 and 10, it is clearly note that the second order slip model shows higher values of the velocity at the upper wall of convergent flow and lesser one at the upper wall of divergent channel. Consequently the backflow phenomenon is entirely disappeared in such situations.

Table 3 delineates, for both convergent and divergent flows, the variation of HNF velocity under the effect of nanoparticles shape factor, m and both velocity-slip models when $\alpha = \pm 3°, Ha = 1000, \varphi_{cu} = \varphi_{Al_2O_3} = 2\%, Kn = 0.04, \sigma_v = 0.6$ and $Re = 220$. Results obtained, show the direct relationship between shape factor and nanofluid velocity where the HNF velocity is clearly improved with the presence of large values of a nanoparticle shape factor in both convergent channel and divergent channel. For these cases, it is highly noticed that the velocity of the hybrid mixture nanoparticles (Cu-Al_2O_3) in the cylindrical form inserted in the mixture $H_2O - C_2H_6O_2$ base fluid displays higher values when compared to the other considered hybrid nanofluids.

5.2. Skin friction coefficient

In this investigation, we are interested on the evolution of SFC at the upper walls (i.e. $\eta = +1$). In fact, it is worth to mention that the negative values of SCF ($F'(1) < 0$) mainly indicate that the backflow is entirely precluded; however, the positive values reveal that the reversal flow appeared.

Effects of Hartmann number and shape factors on local SFC in divergent channel for both slip models are shown in Fig. 11 when $\alpha = 3°$, $\varphi_{cu} = \varphi_{Al_2O_3} = 2\%, \sigma_v = 0.2, Kn = 0.06$ et $Re = 240$. As visualized, local SFC decreases with the augment of both Hartmann number and shape factors, thus signalling the vanishment of backflow phenomenon for both considered velocity-slip boundary conditions models. Fig. 11 also reveals that the minimal local SFC is obtained in the case of hybrid nanofluid with nanoparticles of Platelet form. Also, results obtained show that the local SFC is lower with second-order slip model when compared to that gained with first-order slip model. In fact, we notice a reduction of 43% at Hrtmann number Ha = 200 and a reduction of 50% when the Hartmann number is equal to 1200. The comparison of local SFC in the case of Platelet form when compared to that of spherical form in the case of second-order slip boundary condition demonstrate a low reduction of 7,5 % when Ha = 200 and a higher reduction of 70% when Ha = 1200.

The impact of VF of copper nanoparticles (φ_{cu}) on local SFC for both slip models are drawn in Fig. 12 when $\alpha = 3°, Ha = 0, \varphi_{Al_2O_3} = 2.5\%$, $\sigma_v = 0.2, Kn = 0.06$ et $Re = 240$. In fact, an increase in local SFC is observed with gradual increase in nanoparticles VF φ_{cu} and consequently, the backflow phenomenon is started. On the other hand, as displayed in Fig. 13, under the effect of alumina (Al_2O_3) nanoparticle VF, a lower variation of local SFC for both slip models of boundary conditions in divergent channel was observed which delay the flow separation. Effects of Knudsen number, phase of nanoparticle ($Cu/Al_2O_3 - Cu$) and nature of base fluid ($H_2O/H_2O - C_2H_6O_2$) on local SFC are shown in Figs. 14 and 15 for both slip models in diverging channel when $\alpha = 3°, Ha = 0, \varphi_{cu} = \varphi_{Al_2O_3} = 2\%, \sigma_v = 0.2$ and $Re = 220$. As can be seen, we notice a decrease of local SFC with the increase of Knudsen number and phase of nanoparticle for the considered velocity-slip boundary conditions models. For these cases, it is worth to conclude that he reversal flow can be entirely excluded as the magnitude of Knudsen number increase. Furthermore, it should also be noted that hybrid phase ($Al_2O_3 - Cu$) presents lower local SFC than nano-phase (Cu). Finally, as drawn in Figs. 14 and 15, we can conclude that the same reductions of local SFC intensity was observed when comparing second-order slip model with first-order slip model. In fact, the local SFC with second-order slip model is reduced by 15,2% when Kn = 0,04 and by 69% when Kn = 0,08.

5.3. Comparison and validation

As described in Tables 4-5 and Fig. 16, the DRA solution reveals an excellent and positive agreement with the Runge-Kutta-Fehlberg (RKF-45) solution used as a guide; hence we are confident to use the DRA method as the main tool for the computation of the present problem for both slip models. For the validity and the effectiveness of the DRA technique, a comparison of the present results is made with those reported in literature of M. A. Al-Nimr et al. [46]. In fact, results drawn in Fig. 17 for both slip models match perfectly, demonstrating the higher reliability of the adopted Duan-Rach approach. On the other hand, to justify advantageously the higher accuracy of DRA method, a comparison is also made with results obtained via HAM based Mathematica package BVPh2. In fact, it is highly noticed that the data compared are in perfect agreement.Fig. 18.Fig. 19..

Finally, as exhibited in Table 6, it is highly noticed for both converging–diverging channels, when $\alpha = \pm 3^\circ$, $Ha = 0$, $\varphi_{cu} = \varphi_{Al_2O_3} = 2\%$, $Kn = 0.05$, $\sigma_v = 0.4$ and $Re = 100$ that the accuracy of DRA solution augment with the augment of order of solution approximation (i.e. at the 27 th- order of approximation). In fact, it may be concluded that the order of solution approximation should be chosen to get better solution with less error.

6. Concluding remarks

In this study, we have examined the combined effect of hybrid nanoparticle and velocity slip Boundary Conditions on the nonlinear problem of MHD Jeffery–Hamel flow. The combination of Al_2O_3 (φ_1) and Cu (φ_2) nanoparticles with pure water base fluid and the mixture base fluid $H_2O - C_2H_6O_2$ (50% − 50%) is considered. In this investigation, the governing equations based on the mathematical modeling are transformed into ordinary differential equations and numerically solved by use of Runge-Kutta-Fehlberg 4th–5th order with shooting technique and analytically via Duan–Rach Approach (DRA).

The main key features of the desired problem are as follows.

- In convergent channel, the hybrid nanofluid velocity $F(\eta)$ increments with an augmentation in Re, α Ha, m, Kn and $\varphi_{Al_2O_3+Cu}$ for both velocity-slip boundary conditions models.
- In divergent channel, the hybrid nanofluid velocity $F(\eta)$ increments with an augmentation in Ha and m, while it decrements with increasing Re, α, $\varphi_{Al_2O_3+Cu}$ and Kn for both slip models.
- The Skin friction coefficient C_f decreases with an increase in Ha, m, Kn and the $\varphi_{Al_2O_3}$ while it increases with increasing φ_{Cu}.
- The minimal local SFC is obtained in the case of hybrid nanofluid with nanoparticles of Platelet form.
- A reduction of 50% in the magnitude of local SFC is obtained with second-order slip model when compared to that of first-order slip model when the Hartmann number is equal to 1200.
- In the case of Platelet form nanoparticles and second-order slip model, the local SFC shows a higher reduction of 70% compared to that obtained with nanoparticles of spherical form when Hartmann number Ha = 1200.
- The hybrid phase ($Al_2O_3 - Cu$) presents lower Skin friction coefficient to that obtained for the nano-phase (Cu).
- The mixture base fluid ($H_2O - C_2H_6O_2$) predicts lower Skin friction coefficient C_f than base fluid (H_2O).
- Higher reduction of 69% in local SFC intensity was observed for both hybrid phase ($Al_2O_3 - Cu$) and mixture base fluid ($H_2O - C_2H_6O_2$) with second-order slip boundary conditions when Knudsen number Kn = 0,08.
- It was noticed via comparisons and test of convergence that the DRA method is significantly reliable and robust.

Declaration of Competing Interest

The authors declare that they have no known competing financial interests or personal relationships that could have appeared to influence the work reported in this paper.

Data availability

No data was used for the research described in the article.

References

[1] H. Alfvén, Existence of electromagnetic-hydrodynamic waves, Nature 150 (3805) (1942) 405–406.

[2] G. Zhao, Y. Jian, L. Chang, M. Buren, Magnetohydrodynamic flow of generalized Maxwell fluids in a rectangular micropump under an AC electric field, J. Magn. Magn. Mater. 387 (1) (August 2015) 111–117.

[3] PV.S. Narayana, B. Venkateswarlu, B. Devika, Chemical reaction and heat source effects on MHD oscillatory flow in an irregular channel, Ain Shams Eng. J. 7 (4) (2016) 1079–1088.

[4] A. Shafiq, T.N. Sindhu, Statistical study of hydromagnetic boundary layer flow of Williamson fluid regarding a radiative surface, Results Phys. 7 (2017) 3059–3067.

[5] T. Muhammad, T. Hayat, A. Alsaedi, A. Qayyum, Hydromagnetic unsteady squeezing flow of Jeffrey fluid between two parallel plates, Chin. J. Phys. 55 (4) (2017) 1511–1522.

[6] S. Ahmad, F. Chishtie, A. Mahmood, Analytical technique for magnetohydrodynamic (MHD) fluid flow of a periodically accelerated plate with slippage, Eur. J. Mech.-B/Fluids 65 (2017) 192–198.

[7] K. Mohamed, et al., Heat transfer in hydro-magnetic nano-fluid flow between non-parallel plates using DTM, J. Appl. Comput. Mech. 4 (4) (2018) 352–364.

[8] M.I. Khan, T. Hayat, M.I. Khan, M. Waqas, A. Alsaedi, Numerical simulation of hydromagnetic mixed convective radiative slip flow with variable fluid properties: a mathematical model for entropy generation, J. Phys. Chem. Solid 125 (2019) 153–164.

[9] S. Gherieb, M. Kezzar, A. Nehal, M.R. Sari, A new improved generalized decomposition method (improved-GDM) for hydromagnetic boundary layer flow, Int. J. Numer. Meth. Heat Fluid Flow 30 (10) (2020) 4607–4628.

[10] C.M. Ayeche, M. Kezzar, M.R. Sari, M.R. Eid, Analytical ADM study of time-dependent hydromagnetic flow of biofluid over a wedge, Indian J. Phys. 95 (12) (2021) 2769–2784.

[11] U.S. Mahabaleshwar, T. Maranna, L.M. Pérez, S.N. Ravichandra Nayakar, An effect of magnetohydrodynamic and radiation on axisymmetric flow of non-Newtonian fluid past a porous shrinking/stretching surface, J. Magn. Magn. Mater. 571 (2023), 170538.

[12] K.N. Sneha, G. Bognar, U.S. Mahabaleshwar, D.K. Singh, O.P. Singh, Magnetohydrodynamics effect of Marangoni nano boundary layer flow and heat transfer with CNT and radiation, J. Magn. Magn. Mater. 575 (2023), 170721.

[13] Choi, S. U. S., and Jeffrey A. Eastman. "Enhancing thermal conductivity of fluids with nanoparticles, Argonne National Lab.(ANL), Argonne, IL (United States), 1995." (2022).

[14] S. Akbar, S.N. Noreen, N.F.M. Noor, Free convective MHD peristaltic flow of a jeffrey nanofluid with convective surface boundary condition: a biomedicine-nano model, Curr. Nanosci. 10 (3) (2014) 432–440.

[15] M. Turkyilmazoglu, A note on the correspondence between certain nanofluid flows and standard fluid flows, J. Heat Transfer 137 (2) (2015), 024501.

[16] M. Turkyilmazoglu, Flow of nanofluid plane wall jet and heat transfer, Eur. J. Mech.-B/Fluids 59 (2016) 18–24.

[17] R. Mohebbi, M.M. Rashidi, Numerical simulation of natural convection heat transfer of a nanofluid in an L-shaped enclosure with a heating obstacle, J. Taiwan Inst. Chem. Eng. 72 (2017) 70–84.

[18] F. Garoosi, M.M. Rashidi, Two phase flow simulation of conjugate natural convection of the nanofluid in a partitioned heat exchanger containing several conducting obstacles, Int. J. Mech. Sci. 130 (2017) 282–306.

[19] M.R. Sari, M. Kezzar, R. Adjabi, Heat transfer of copper/water nanofluid flow through converging-diverging channel, J. Cent. South Univ. 23 (2) (2016) 484–496.

[20] M. Kezzar, M.R. Sari, "Series solution of nanofluid flow and heat transfer between stretchable/shrinkable inclined walls.", Int. J. Appl. Comput. Math. 3 (2017) 2231–2255.

[21] X. Yin, C. Hu, M. Bai, J. Lv, An investigation on the heat transfer characteristics of nanofluids in flow boiling by molecular dynamics simulations, Int. J. Heat Mass Transf. 162 (2020) 120338.

[22] A.V. Minakov, D.V. Guzei, K.N. Meshkov, I.A. Popov, A.V. Shchelchkov, Experimental study of turbulent forced convection of nanofluid in channels with cylindrical and spherical hollows, Int. J. Heat Mass Transf. 115 (2017) 915–925.

[23] G.J. Tertsinidou, C.M. Tsolakidou, M. Pantzali, M.J. Assael, L. Colla, L. Fedele, S. Bobbo, W.A. Wakeham, New measurements of the apparent thermal conductivity of nanofluids and investigation of their heat transfer capabilities, J. Chem. Eng. Data 62 (1) (2017) 491–507.

[24] S. Mukherjee, S. Jana, P. Chandra Mishra, P. Chaudhuri, S. Chakraborty, Experimental investigation on thermo-physical properties and subcooled flow boiling performance of Al2O3/water nanofluids in a horizontal tube, Int. J. Therm. Sci. 159 (2021), 106581.

[25] A. Belazreg, I.L. Animasaun, A. Abderrahmane, S. Mohammed, K. Guedri, B. M. Fadhl, Q.M. Al-Mdallal, Insight into latent heat thermal energy storage: RT27 phase transition material conveying copper nanoparticles experiencing entropy generation with four distinct stepped fin surfaces, Int. J. Thermofluids 19 (2023), 100368.

[26] H. Vaidya, I.L. Animasaun, K.V. Prasad, C. Rajashekhar, J.U. Viharika, Q.M. Al-Mdallal, Nonlinear dynamics of blood passing through an overlapped stenotic artery with copper nanoparticles, J. Non-Equilib. Thermodyn. 48 (2) (2023) 159–178.

[27] J. Sarkar, P. Ghosh, A. Adil, A review on hybrid nanofluids: recent research, development and applications, Renew. Sustain. Energy Rev. 43 (2015) 164–177.

[28] M. Hemmat Esfe, A.A. Abbasian Arani, M. Rezaie, W.-M. Yan, A. Karimipour, Experimental determination of thermal conductivity and dynamic viscosity of Ag–MgO/water hybrid nanofluid, Int. Commun. Heat Mass Transfer 66 (2015) 189–195.

[29] D. Huang, W.u. Zan, B. Sunden, Effects of hybrid nanofluid mixture in plate heat exchangers, Exp. Therm Fluid Sci. 72 (2016) 190–196.

[30] M. Mehrali, E. Sadeghinezhad, A.R. Akhiani, S. Tahan Latibari, H.S.C. Metselaar, A. S. Kherbeet, M. Mehrali, Heat transfer and entropy generation analysis of hybrid

graphene/Fe3O4 ferro-nanofluid flow under the influence of a magnetic field, Powder Technol. 308 (2017) 149–157.

[31] A.J. Chamkha, A.S. Dogonchi, D.D. Ganji, Magneto-hydrodynamic flow and heat transfer of a hybrid nanofluid in a rotating system among two surfaces in the presence of thermal radiation and Joule heating, AIP Adv. 9 (2) (2019).

[32] I. Waini, A. Ishak, I. Pop, Flow and heat transfer of a hybrid nanofluid past a permeable moving surface, Chin. J. Phys. 66 (2020) 606–619.

[33] K. Muhammad, et al., Mixed convective slip flow of hybrid nanofluid (MWCNTs+ Cu+ Water), nanofluid (MWCNTs+ Water) and base fluid (Water): a comparative investigation, J. Therm. Anal. Calorim. 143 (2021) 1523–1536.

[34] I.L. Animasaun, A.S. Oke, Q.M. Al-Mdallal, A.M. Zidan, Exploration of water conveying carbon nanotubes, graphene, and copper nanoparticles on impermeable stagnant and moveable walls experiencing variable temperature: thermal analysis, J. Therm. Anal. Calorim. 148 (10) (2023) 4513–4522.

[35] S. Saranya, et al., Quartic autocatalysis on horizontal surfaces with an asymmetric concentration: water-based ternary-hybrid nanofluid carrying titania, copper, and alumina nanoparticles, Phys. Scr. (2023).

[36] G.B. Jeffery, The two-dimensional steady motion of a viscous fluid, Russian J. Nonlinear Dyn. 5 (1) (2009) 101–109.

[37] G. Hamel, Spiralförmige Bewegungen zäher Flüssigkeiten, Jahresber. Deutsch. Math.-Verein. 25 (1917) 34–60.

[38] L. Rosenhead, The steady two-dimensional radial flow of viscous fluid between two inclined plane walls, Proc. R. Soc. Lond. A 175 (963) (1940) 436–467.

[39] Fraenkel, Ludwig Edward, and Herbert Brian Squire. "Laminar flow in symmetrical channels with slightly curved walls, I. On the Jeffery-Hamel solutions for flow between plane walls." *Proceedings of the Royal Society of London. Series A. Mathematical and Physical Sciences* 267.1328 (1962): 119-138.

[40] K. Millsaps, K. Pohlhausen, Thermal distributions in Jeffery-Hamel flows between nonparallel plane walls, J. Aeronaut. Sci. 20 (3) (1953) 187–196.

[41] P.M. Eagles, The stability of a family of Jeffery-Hamel solutions for divergent channel flow, J. Fluid Mech. 24 (1) (1966) 191–207.

[42] I.J. Sobey, P.G. Drazin, Bifurcations of two-dimensional channel flows, J. Fluid Mech. 171 (1986) 263–287.

[43] M. Hamadiche, J. Scott, D. Jeandel, Temporal stability of Jeffery-Hamel flow, J. Fluid Mech. 268 (1994) 71–88.

[44] F.J. Uribe, E. Díaz-Herrera, A. Bravo, R. Peralta-Fabi, On the stability of the Jeffery-Hamel flow, Phys. Fluids 9 (9) (1997) 2798–2800.

[45] M.R. Jotkar, R. Govindarajan, Non-modal stability of Jeffery-Hamel flow, Phys. Fluids 29 (6) (2017).

[46] Al-Nimr, M. A., Vladimir A. Hammoudeh, and M. A. Hamdan. "Effect of velocity-slip boundary conditions on Jeffery–Hamel flow solutions." (2010): 041010.

[47] L. Wu, A slip model for rarefied gas flows at arbitrary Knudsen number, Appl. Phys. Lett. 93 (25) (2008).

[48] S. Fukui, R. Kaneko, Dynamic analysis of flying head sliders with ultra-thin spacing based on the Boltzmann equation: Comparison with two limiting approximations, JSME Int J III. 33 (1) (1990) 76–85.

[49] A. Salman, C. Farrukh, M. Asad, Analytical technique for magnetohydrodynamic (MHD) fluid flow of a periodically accelerated plate with slip, Eur. J. Mech. B/ Fluids 65 (2017) 192–198.

[50] A. Martins Obalalu, The influence of variable electrical conductivity on non-Darcian Casson nanofluid flow with first and second-order slip conditions, Partial Differ. Equations Appl. Math. 4 (2021), 100084.

[51] A.S.M. Aljaloud, L. Manai, I. Tlili, "Bioconvection flow of Cross nanofluid due to cylinder with activation energy and second order slip features.", Case Studies Therm. Eng. 42 (2023), 102767.

[52] S. Liao, Beyond perturbation: introduction to the homotopy analysis method, CRC Press, 2003.

[53] S.-J. Liao, K.F. Cheung, Homotopy analysis of nonlinear progressive waves in deep water, J. Eng. Math. 45 (2003) 105–116.

[54] J.-H. He, Variational iteration method—some recent results and new interpretations, J. Comput. Appl. Math. 207 (1) (2007) 3–17.

[55] G. Adomian (Ed.), Solving Frontier Problems of Physics: The Decomposition Method, Springer Netherlands, Dordrecht, 1994.

[56] J.-S. Duan, R. Rach, A new modification of the Adomian decomposition method for solving boundary value problems for higher order nonlinear differential equations, Appl. Math Comput. 218 (8) (2011) 4090–4118.

[57] A. Dib, A. Haiahem, B. Bou-Said, An analytical solution of the MHD Jeffery-Hamel flow by the modified Adomian decomposition method, Comput. Fluids 102 (2014) 111–115.

[58] A.S. Dogonchi, D.D. Ganji, Impact of Cattaneo-Christov heat flux on MHD nanofluid flow and heat transfer between parallel plates considering thermal radiation effect, J. Taiwan Inst. Chem. Eng. 80 (2017) 52–63.

[59] A.S. Dogonchi, D.D. Ganji, Analytical solution and heat transfer of two-phase nanofluid flow between non-parallel walls considering Joule heating effect, Powder Technol. 318 (2017) 390–400.

[60] M. Kezzar, N. Boumaiza, I. Tabet, N. Nafir, Combined effects of ferromagnetic particles and magnetic field on mixed convection in the Falkner-Skan system using DRA, Int. J. Numer. Meth. Heat Fluid Flow 29 (2) (2019) 814–832.

[61] M. Gahgah, M.R. Sari, M. Kezzar, M.R. Eid, Duan–Rach modified Adomian decomposition method (DRMA) for viscoelastic fluid flow between nonparallel plane walls, Eur. Phys. J. Plus 135 (2) (2020).

[62] M. Kezzar, I. Tabet, M.R. Eid, A new analytical solution of longitudinal fin with variable heat generation and thermal conductivity using DRA, Eur. Phys. J. Plus 135 (1) (2020) 1–15.

[63] W. Fenizri, M. Kezzar, M.R. Sari, I. Tabet, M.R. Eid, New modified decomposition method (DRMA) for solving MHD viscoelastic fluid flow: comparative study, Int. J. Ambient Energy 43 (1) (2022) 3686–3694.